Geophysical Journal International

Geophys. J. Int. (2017) **210,** 1070–1091
Advance Access publication 2017 May 12
GJI Geodynamics and tectonics

doi: 10.1093/gji/ggx209

Crustal deformation induced by mantle dynamics: insights from models of gravitational lithosphere removal

Huilin Wang[1,2] and Claire A. Currie[1]

[1]*Department of Physics, University of Alberta, Edmonton, AB T6G 2E1, Canada*
[2]*Seismological Laboratory, California Institute of Technology, Pasadena, CA 91125, USA. E-mail: huilin@gps.caltech.edu*

Accepted 2017 May 11. Received 2017 May 10; in original form 2016 December 13

SUMMARY

Mantle-based stresses have been proposed to explain the occurrence of deformation in the interior regions of continental plates, far from the effects of plate boundary processes. We examine how the gravitational removal of a dense mantle lithosphere root may induce deformation of the overlying crust. Simplified numerical models and a theoretical analysis are used to investigate the physical mechanisms for deformation and assess the surface expression of removal. Three behaviours are identified: (1) where the entire crust is strong, stresses from the downwelling mantle are efficiently transferred through the crust. There is little crustal deformation and removal is accompanied by surface subsidence and a negative free-air gravity anomaly. Surface uplift and increased free-air gravity occur after the dense root detaches. (2) If the mid-crust is weak, the dense root creates a lateral pressure gradient in the crust that drives Poiseuille flow in the weak layer. This induces crustal thickening, surface uplift and a minor free-air gravity anomaly above the root. (3) If the lower crust is weak, deformation occurs through pressure-driven Poiseuille flow and Couette flow due to basal shear. This can overthicken the crust, producing a topographic high and a negative free-air gravity anomaly above the root. In the latter two cases, surface uplift occurs prior to the removal of the mantle stress. The modeling results predict that syn-removal uplift will occur if the crustal viscosity is less than $\sim 10^{21}$ Pa s, corresponding to temperatures greater than ∼400–500 °C for a dry and felsic or wet and mafic composition, and ∼900 °C for a dry and mafic composition. If crustal temperatures are lower than this, lithosphere removal is marked by the formation of a basin. These results can explain the variety of surface expressions observed above areas of downwelling mantle. In addition, observations of the surface deflection may provide a way to constrain the vertical rheological structure of the crust.

Key words: Dynamics of lithosphere and mantle; Intra-plate processes; Rheology: crust and lithosphere; Tectonics and landscape evolution.

1 INTRODUCTION

Crustal deformation and vertical surface deflection have been observed in the interior regions of many continental plates. These range from the creation of sedimentary basins (e.g. the Congo basin in Africa and the Tulare basin in North America; Downey & Gurnis 2009; Levandowski & Jones 2015) to the formation of mountains (e.g. the Tien Shan in China and the Alpine and Carpathian orogens in Europe; Houseman & Molnar 2001; Gemmer & Houseman 2007). Such events contrast with the traditional view of rigid tectonic plate, where deformation is limited to plate boundaries (e.g. Kreemer *et al*. 2003). Two main causes have been proposed to explain intraplate deformation: (1) stresses transmitted laterally from plate boundaries that localize in weak intraplate regions (e.g. Kusznir & Park 1984; Mazzotti & Hyndman 2002); and (2) stresses transmitted upwards from the dynamic mantle (e.g. McKenzie 1977; Neil & Houseman 1999). Mechanism (2) includes stresses originating from either the sublithospheric mantle or the mantle lithosphere. In either case, the mantle-based stresses may result in deformation of the overlying crust and/or deflection of the Earth's surface (e.g. Morgan 1965; Neil & Houseman 1999; Buiter *et al*. 2002; Pysklywec & Shahnas 2003; Burov & Guillou-Frottier 2005; Burov & Cloetingh 2009; Duretz *et al*. 2012; Flament *et al*. 2013). Within the sublithospheric mantle, downwelling (e.g. a region of subduction) or upwelling (e.g. a mantle plume) impose vertical stresses on the upper plate and may depress or uplift the Earth's surface by hundreds of metres over wavelengths of hundreds to thousands of kilometres (Gurnis *et al*. 1998; Burov & Guillou-Frottier 2005; Burov & Cloetingh 2009; Braun 2010; Flament *et al*. 2013). On the other hand, dynamical processes in the mantle lithosphere may

induce deformation on shorter wavelengths. For example, crustal deformation and surface deflection over tens to hundreds of kilometres are observed above regions associated with foundering mantle lithosphere (e.g. the Arizaro basin in the central Andes; Schoenbohm & Carrapa 2014).

In this study, we investigate the relationship between gravitational lithosphere removal and crustal deformation in order to understand how mantle-based stresses are transferred through the crust, inducing deformation and deflection of the overlying surface. The mantle lithosphere may be denser than the underlying mantle because of its lower temperature and/or the presence of dense compositions (e.g. eclogite) produced through magmatic and metamorphic processes. As a result, the mantle lithosphere can be 20–300 kg m^{-3} denser and thus is susceptible to gravitational foundering into the deeper mantle (e.g. Houseman *et al*. 1981; Kay & Kay 1993; Ducea & Saleeby 1996; Poudjom Djomani *et al*. 2001; Jull & Kelemen 2001; Richards 2003; Saleeby *et al*. 2003). On the basis of seismic tomography images, sedimentation records, magmatic history and other observations, lithosphere removal is inferred to have occurred in a number of regions, such as the Puna Plateau in South America (Ducea *et al*. 2013), the Tien Shan orogen in Asia (Houseman & Molnar 2001) and the southern Appalachian orogen in North America (Biryol *et al*. 2016).

A variety of surface expressions are observed over regions of proposed gravitational lithosphere removal. The formation of a dense lithosphere root is expected to cause isostatically driven subsidence, followed by surface uplift as the root detaches. There may also be a dynamic component of surface deflection, as root foundering and subsequent mantle upwelling induce vertical stresses on the overlying material. These processes may explain the development of transient sedimentary basins (depth $>$ 0.5 km), such as the Tulare basin in the western California (Saleeby *et al*. 2012) and the Arizaro basin in the central Andes (Wang *et al*. 2015). However, there are places where lithosphere removal is associated with either minor surface subsidence (depth $<$ 0.5 km) or surface uplift (ranging from hundreds to thousands of metres). These include the Wallowa Mountains in North America (Hales *et al*. 2005), the Tien Shan orogen in China (Houseman & Molnar 2001), the Isan orogen in Australia (Pysklywec & Beaumont 2004) and the Rif mountain in northern Morocco (Petit *et al*. 2015).

The diverse surface deflections associated with lithosphere removal appear to be related to crustal deformation, as removal induces stresses within the overlying crust. A number of studies have used linear stability analysis to assess crustal deformation during gravitational removal, assuming either a single-layer viscous crust (e.g. Neil & Houseman 1999; Molnar & Houseman 2013) or one with an exponential decrease in viscosity with depth (Molnar & Houseman 2015). These studies demonstrate if the crust is relatively strong ($>$13–30 times more viscous than mantle), lithosphere removal is accompanied by surface subsidence. If the crust is weaker, the mantle downwelling causes contraction and thickening in the overlying crust, leading to surface uplift. These analyses provide an instantaneous picture of the surface and Moho deflection associated with a small-amplitude perturbation at the base of the dense lithosphere. Other studies have considered the time-dependent evolution of lithosphere removal below a single-layer crust with either a constant viscosity (e.g. Neil & Houseman 1999; Pysklywec & Shahnas 2003; Hoogenboom & Houseman 2006) or variable viscosity (e.g. Elkins-Tanton 2007; Gemmer & Houseman 2007; Göğüş & Pysklywec 2008), or a two-layer crust with a variable viscosity (e.g. Wang *et al*. 2014, 2015). These models also demonstrate the occurrence of crustal deformation in areas where the crust is relatively weak, leading to crustal thickening and surface uplift above the foundering lithosphere. An important result of these models is that the surface uplift occurs prior to the detachment of the dense lithosphere, contrary to what would be expected for rigid plates.

These studies highlight that the potential importance of crustal deformation in modifying the surface expression of lithosphere removal. The majority of studies cited above consider the crust as a single viscous layer. In contrast, rheological studies show that the crust may be vertically stratified (e.g. Burov & Guillou-Frottier 2005; Burov & Watts 2006). In particular, there may be weak layers within the mid- or lower crusts, and deformation should preferentially localize in these layers. In our previous work, we found that the crustal behaviour during lithosphere removal is sensitive to the rheological layering in the crust (Wang *et al*. 2014, 2015). However, these models use a non-Newtonian, temperature-dependent rheology for each crustal layer. The complex feedback among strain rate, temperature and effective viscosity make it difficult to access the fundamental physical mechanisms that drive crustal deformation.

In this study, we use simplified numerical models with a layered crustal viscosity to evaluate that how gravitational lithosphere removal may induce crustal deformation. Specifically, we investigate how the presence of a weak crustal layer affects the deformation and the resulting surface expression (topography and gravity; Fig. 1a). By using simplified models, we can compare the model results with a theoretical analysis to demonstrate the factors that drive deformation. This approach provides insight into the origin of crustal deformation induced by mantle stresses, and therefore the results are relevant to other areas where the convective mantle exerts a stress on the crust.

2 CRUSTAL VISCOSITY STRUCTURE

Geological and geophysical studies show that the crust has a multilayered rheological structure, and in some cases there may be a weak viscous channel in the mid- or lower crusts (Burov & Watts 2006; Royden *et al*. 2008). One place where a weak mid-crustal channel may exist is southern Tibet. Reflection bright spots in seismic studies (Makovsky *et al*. 1996; Nelson *et al*. 1996) and high electrical conductivities in a magnetotelluric study (Li *et al*. 2003) are interpreted to indicate a weak channel at 15–40 km depth; the crustal thickness in this area is ∼70 km. The electrical conductance suggests viscosities of 2.5 $\times$ 10^{18}–3 $\times$ 10^{20} Pa s in this channel (Rippe & Unsworth 2010). In other places, a weak channel has been inferred in the lower crust. For example, an analysis of the topographic evolution of the central Andes suggests that there may be a ∼30 km thick weak layer with a viscosity of 10^{19}–10^{20} Pa s that extends to the base of the ∼65 km thick crust (Gerbault *et al*. 2005). At the boundaries of the Tibetan plateau, a 15 km thick weak lower crust (viscosity of 10^{18}–10^{21} Pa s) can explain the gradients in surface topography (Clark & Royden 2000). In the Basin and Range province of the western United States, long-wavelength gravity anomalies and topographies are consistent with a 25 km thick lower-crustal channel with a viscosity of 10^{18}–10^{20} Pa s (Kruse *et al*. 1991).

A low-viscosity channel can occur because the viscous strength of crustal rocks decreases with temperature (e.g. Kohlstedt *et al*. 1995; Ranalli 1995). To demonstrate the general conditions under which a weak crustal layer may form, we have calculated viscous strength profiles (Fig. 1). The calculations use a 60 km thick crust, comparable to the thickness in orogenic regions where crustal channels are

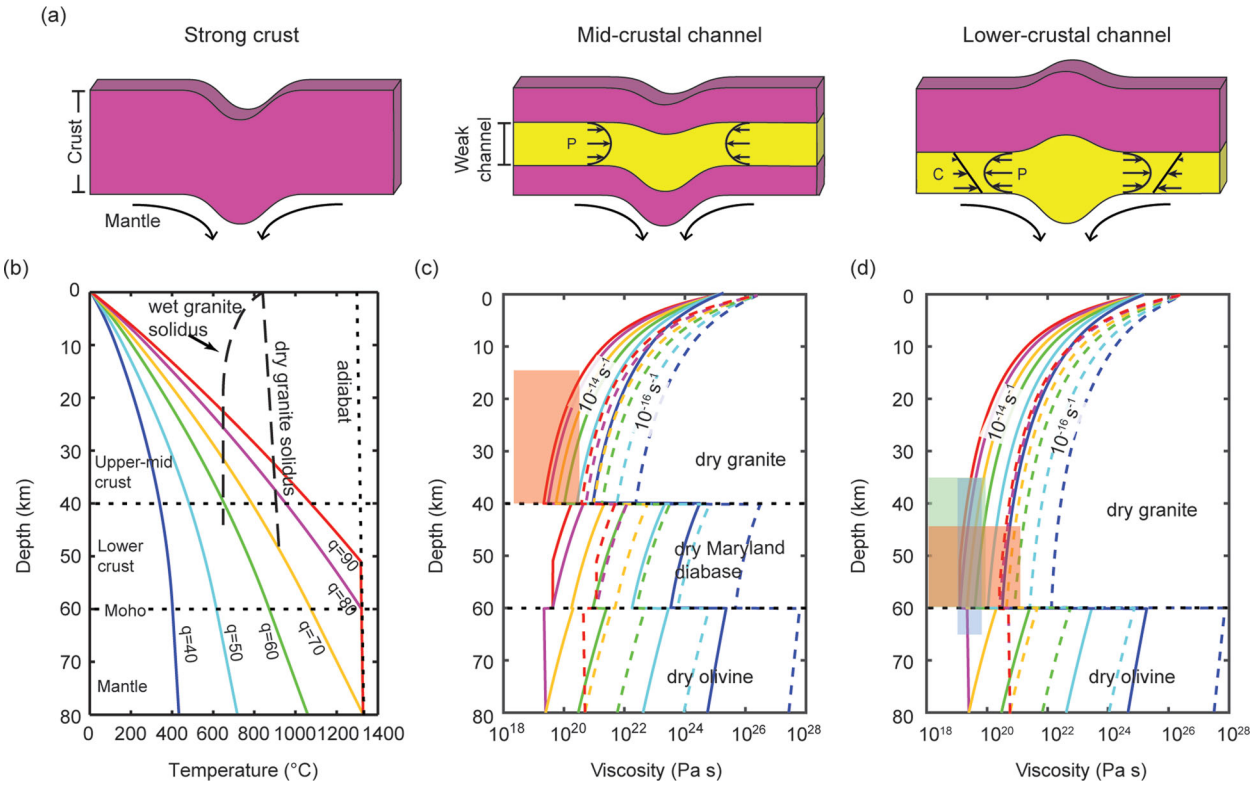

Figure 1. (a) Illustration of surface deformation and flow in a weak crustal channel (yellow) induced above a mantle downwelling. P = Poiseuille flow. C = Couette flow. (b) Geotherms for a 60 km crust, consisting of a 40 km upper-mid crust and 20 km lower crust. The geotherm profiles correspond to different surface heat flows (q, in mW m^{-2}). These are calculated with a thermal conductivity of 2.5 Wm^{-1} K^{-1} for all materials and radiogenic heat production of 1.3 μW m^{-3} in the top 10 km of the crust, 0.4 μW m^{-3} in the rest of the crust and 0 μW m^{-3} in the mantle (Currie *et al*. 2004). The dry and wet granite solidus lines are from Chapman (1986). (c) Effective viscosity profiles calculated for each geotherm [using same line colours as in (b)], assuming a felsic upper-mid crust and mafic lower crust. Rheology parameters for upper-mid crust are those of dry granite (Ranalli 1995), the lower crust uses dry Maryland diabase parameters (Mackwell *et al*. 1998), and the mantle uses dry olivine parameters (Hirth & Kohlstedt 1996). The red rectangle shows the inferred depth and viscosity for a mid-crustal channel in southern Tibet (see the main text). (d) Effective viscosity profiles assuming that the entire crust is felsic, with the rheology parameters of dry granite (Ranalli 1995). The red rectangle is the depth and viscosity of the inferred lower-crustal channel at the edge of Tibet (Clark & Royden 2000); the green rectangle shows the conditions for the lower-crust channel under Nevada (Kruse *et al*. 1991); the blue line shows the depths and viscosity in the central Andean plateau (Gerbault *et al*. 2005). The effective viscosity calculations use a strain rate of 10^{-14} s^{-1} (solid lines) and 10^{-16} s^{-1} (dashed lines).

observed. Strength profiles are calculated for the geotherms shown in Fig. 1(b), corresponding to surface heat flows of 40–90 mW m^{-2}. A heat flow greater than 70 mW m^{-2} gives extremely high temperatures in deep crust, and therefore temperatures are capped at those of a 1300 °C adiabat.

Fig. 1(c) shows the predicted strength profiles for crust consisting of a felsic upper-mid crust and a mafic lower crust (Ranalli & Murphy 1987), using the rheological parameters of dry granite (Ranalli 1995) and dry Maryland diabase (Mackwell *et al*. 1998), respectively. Fig. 1(d) shows the strength profiles assuming that the entire crust is felsic (Gao *et al*. 1998) and has a dry granite rheology (Ranalli 1995). Hydration and partial melting will result in lower effective viscosities than shown in Figs 1(c) and (d) (e.g. Rosenberg & Handy 2005). In the calculations, strain rates of 10^{-14}–10^{-16} s^{-1} are used, as the crustal strain rates in the numerical models in Section 3 generally fall within this range, with the weak channel having a higher strain rate. In the following, we assume that a weak channel is created if the viscosity is less than 10^{21} Pa s over a thickness of at least 10 km, and the weak channel is taken to deform at 10^{-14} s^{-1}.

Fig. 1(c) shows that to create a weak mid-crustal channel, the crust must have a layered composition such that the mid-crust is felsic, while the lower crust is mafic and strong. For a strain rate of 10^{-14} s^{-1}, a weak channel can occur where mid-crustal temperatures are >400 °C, and therefore geotherms for a heat flow greater than 50 mW m^{-2} meet this condition. The mid-crustal channel also requires that the lower crust is strong (viscosity $>10^{21}$ Pa s), which likely requires a dry and mafic lower crust (Fig. 1c). This corresponds to heat flow lower than 70 mW m^{-2}, assuming a low strain rate in this layer (10^{-16} s^{-1}). A higher strain rate, more felsic or more hydrated lower crust would be weaker, and therefore lower temperatures (lower heat flow) would be required to maintain a strong lower crust.

To create a lower-crustal channel, either the lower crust must be warm and felsic, or hot and mafic. For a strain rate of 10^{-14} s^{-1}, this occurs for heat flow greater than 40 mW m^{-2} for felsic lower crust (Fig. 1d), and heat flow greater than 60 mW m^{-2} for mafic lower crust (Fig. 1c). Overall, these calculations demonstrate that a weak channel may form in the mid- or lower crusts in an orogenic region with moderate- to high-surface heat flow. If the crust were thinner than 60 km, higher heat flows are required to attain the critical temperatures needed for a weak channel.

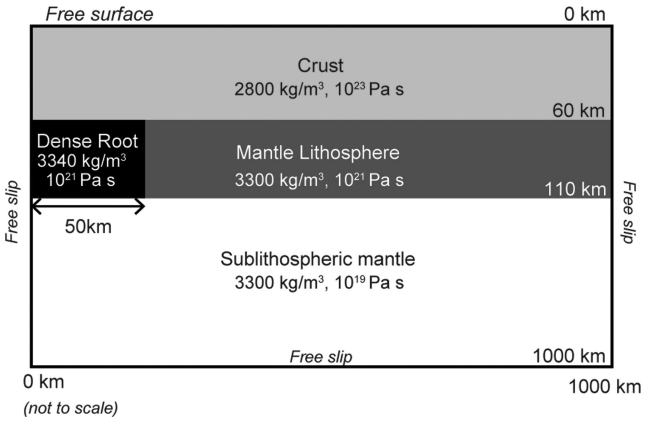

Figure 2. Numerical model geometry and boundary conditions for Model A (see the text for details). For Models B and C, a weak channel with a viscosity of 10^{18} Pa s is placed within the crust at 30–40 and 50–60 km depths, respectively.

3 NUMERICAL MODELS OF LITHOSPHERE REMOVAL

3.1 Numerical model setup

The goal of this study is to assess how the crust behaves during gravitational lithosphere removal. In particular, we are interested in how deformation may concentrate within a weak layer in the mid- or lower crusts. The 2-D numerical models are 1000 km wide and 1000 km deep, with a 110 km thick continental plate (60 km crust and 50 km mantle lithosphere) that overlies sublithospheric mantle (Fig. 2). The side and basal boundaries are free slip, and no material passes through them. The top boundary is stress-free, allowing topography to develop during model evolution.

All layers in the models are initially horizontal and have a constant density and viscosity (Fig. 2 and Table 1). The simplified structure provides a straightforward way to investigate the first-order physical mechanisms for crustal deformation (e.g. Kruse *et al*. 1991; Clark & Royden 2000). The constant viscosity in each layer ensures that only vertical strength variations affect the dynamics. The constant density means that the lateral variation in crustal thickness is one of main factors that controls the deformation and associated surface topography, and precludes complications due to other factors (e.g. temperature effects). These simplifications also allow for an analytical study of the linkage between mantle dynamics, crustal flow and surface topography.

We examine three different crustal structures. In Model A, the crust has a constant viscosity of 10^{23} Pa s, representing the case where the whole crust strong, perhaps due to cool and mafic conditions; lower viscosities are considered in Section 3.3. We then present models with a 10 km thick, low viscosity (10^{18} Pa s) layer in either the mid-crust (Model B) or lower crust (Model C). These models represent end-member cases to demonstrate the effects of an extremely weak channel within the crust. Section 5 examines variations in the channel viscosity and the thickness of the crust and channel.

Gravitational lithosphere removal is initiated by introducing a 50 × 50 km high-density body (root) in the mantle lithosphere that is 40 kg m^{-3} denser than the underlying mantle; in Section 5, variations in root density are considered. As convective drip-style removal is symmetric, only half of the removal is modeled, with the left model boundary being the line of symmetry. As discussed above, the dense root could represent an area with an accumulation of high-density assemblages associated with metamorphic or magmatic processes. The growth rate of a gravitational instability depends on both the density and viscosity of the materials (e.g. Houseman *et al*. 1981; Houseman & Molnar 1997). For simplicity, we do not vary the viscosities of the mantle lithosphere and sublithospheric mantle (Fig. 2); these viscosities are chosen to obtain lithosphere removal on a timescale of 10–20 Ma.

The numerical models use finite-element code SOPALE to calculate the mechanical evolution of crust and mantle under the assumptions of incompressibility and plane strain (Fullsack 1995). SOPALE has been widely used to model crustal channel flow (e.g. Beaumont *et al*. 2001, 2004, 2006; Jamieson *et al*. 2004, 2006). The code uses an arbitrary Lagrangian–Eulerian approach to solve the equations of conservation of mass and force balance. The Eulerian mesh has a resolution of 5 × 2.5 km (width × height) in the upper 140 km, except at 30–60 km depth where the Eulerian mesh is 5 × 1 km. The smaller elements here ensure adequate resolution of the dynamics of the weak channel. In the lower 860 km, the mesh is 5 × 10 km. Benchmark tests show that this resolution is sufficient to resolve growth rates of Rayleigh–Taylor instabilities to within 6 per cent of their expected value (e.g. Houseman & Molnar 1997).

The models are run in two phases. In phase 1, the models are run for 1 Myr without a weak crustal channel. This allows the model to isostatically adjust to the load of dense root. This causes the

Table 1. List of numerical models. In all models, the properties of the strong crust, mantle lithosphere and sublithospheric mantle are those in Fig. 2.

Crustal thickness (km)	Channel depth (km)	Mantle lithosphere thickness (km)	Root density (kg m^{-3})	Channel viscosity (Pa s)	Model
60	No channel	50	3340	n/a	Model A (Fig. 3)
					Crustal viscosity tests (Fig. 5)
	30–40 (MC[a])	50	3340	10^{18}	Model B (Fig. 7)
			3320–3540 (see Section 5)	10^{18}–10^{21} (see Section 5)	Parameter tests (Fig. 10)
	50–60 (LC[b])	50	3340	10^{18}	Model C (Fig. 8)
			3320–3540 (see Section 5)	10^{18}–10^{21} (see Section 5)	Parameter tests (Fig. 11)
40[c]	17–27 (MC[a])	50	3340	10^{18}	
	30–40 (LC[b])	50	3340	10^{18}	

[a]MC = mid-crust channel model.
[b]LC = lower-crust channel model.
[c]For models with 40 km thick crust, the Eulerian mesh has a resolution of 5 × 2.5 km (horizontal × vertical) in the upper 140 km, except at 20–50 km depth where the Eulerian mesh is 5 × 1 km. In the lower 860 km, the mesh is 5 × 10 km.

surface above the root to subside by ∼0.3 km, forming a basin with a half-width of ∼150 km. Model experiments start at this point, which is defined as a time of 0 Myr in the discussion below. In the second phase, we introduce the weak crustal channel to examine how this affects the model evolution. Specifically, we are interested in the crustal flow and associated surface observables (surface topography, crustal thickness and free-air gravity). The flow velocity and thickness of crust and surface topography are obtained directly from the numerical models. To obtain the free-air gravity, the model domain is gridded into rectangular cells, and the gravitational attraction of each cell is calculated at an elevation of 2 km above the undisturbed model surface using the Talwani *et al*. (1959) method. The resulting gravity profile is subtracted from the gravity expected for a lithosphere with a 60 km crust and no dense root, and the gravity difference is corrected for measurement elevation. The resulting profile is therefore the free-air gravity anomaly at an elevation of 0 km.

3.2 Reference models

3.2.1 Strong crust model (Model A)

We first examine lithosphere removal with a strong crust that has a uniform viscosity (10^{23} Pa s), that is, no weak crustal channel. Fig. 3 shows the model evolution. The root is gravitationally unstable and it descends, forming a drip shape at the base of lithosphere by 14 Myr. This is followed by necking and detachment at ∼21 Myr, which removes the majority of the high-density root (Fig. 3c). Here, detachment is used to denote when the coupling between the root and crust rapidly decreases. It corresponds to a rapid increase in the downward velocity of the root (Fig. 3d) and abrupt surface uplift (Fig. 4a). Because of viscous coupling, the uppermost part of the root remains below the crust (Conrad & Molnar 1999), and a tailing conduit remains between the drip and the base of lithosphere (Whitehead & Luther 1975, Fig. 3c).

Fig. 3(a) shows the surface topography, and Fig. 4(a) shows the evolution of surface elevation above the root centre. Throughout the removal process, there is a basin above the drip, with an adjacent small topographic high due to viscous resistance. The basin depth increases from ∼0.3 to ∼0.4 km as the root detaches. This slow subsidence is caused by the dynamic stress from the sinking root. As dense root detaches at ∼21 Myr, the surface uplifts rapidly. At 30 Myr, the basin centre is ∼0.1 km lower than the surroundings; this is due to the presence of the residual dense root in lithosphere.

The gravitational removal affects the free-air gravity. Fig. 3(b) shows that the free-air gravity profile follows that of the surface topography. A negative free-air gravity anomaly is observed above the root and a small positive anomaly is observed over the adjacent topographic high. Over the basin, the negative anomaly increases as the root sinks, and after detachment, the magnitude of the anomaly decreases. The topography is the main contribution to the free-air gravity anomaly. The density contrast between crust and air (2800 kg m^{-3}) means that a topographic low results in a density deficit and thus a negative gravity anomaly. The crustal thickness does not change during the model evolution, and the dense root has a minor contribution to the surface gravity owing to its large depth and its small density contrast relative to the adjacent mantle (40 kg m^{-3}).

Fig. 3(e) shows the horizontal velocities along a vertical profile through the crust at a distance of 150 km (i.e. the edge of the basin). The velocity is zero throughout the root removal process, indicating that there is no internal crustal deformation and the crustal thickness does not change (Fig. 4d). As a result, root removal is associated with surface subsidence and negative free-air gravity. Surface uplift and an increase in free-air gravity only occur after the dense root detaches.

For comparison, we also test models with a lower viscosity crust. With a crustal viscosity of 10^{18} Pa s, the root is weakly coupled to the overlying crust and it founders more rapidly than in Model A, detaching at ∼10 Myr (Fig. 5a). The surface above the root, which was initially a topographic low, undergoes rapid uplift to ∼0 km elevation within ∼1 Myr and remains at this elevation as the root detaches (Figs 4a and 5a). The surface uplift is due to the fact that the dense root induces deformation and thickening of the overlying crust (Fig. 4d, *cf.* Neil & Houseman 1999). The initial isostatic subsidence and negative dynamic topography created by the downwelling mantle are counteracted by the crustal thickening.

Figs 6(a) and (b) show the distribution of stress and strain rate for the models with strong (10^{23} Pa s) and weak (10^{18} Pa s) crust. When the entire crust is strong (Model A), the vertical normal stresses associated with the instability in the mantle are efficiently transferred through the crust, resulting in stresses of $\sim 10^7$ Pa in the crust above the root region. The stresses from downwelling mantle depress the surface above the root, while the crust itself is too strong to deform (strain rates less than 10^{-16} s^{-1}). On the other hand, with a weak crust, stresses are $< 10^4$ Pa in the crust above the root (Fig. 6b). The mantle stresses induce a higher strain rate in the crust ($>10^{-15}$ s^{-1}; Fig. 6b) and the weak crust undergoes thickening above the root. Owing to the weak crust, the surface stresses and topography are decoupled from the underlying lithosphere dynamics.

If the crust has an intermediate viscosity (10^{21} Pa s), root removal induces crustal deformation and thickening, and the surface above the root uplifts to a positive topography of ∼0.25 km prior to root detachment at ∼17 Myr (Figs 4a and 5b). In this model, the crust is thickened by up to ∼8 km prior to detachment, compared to ∼6 km of thickening for the model with the weakest crust (Fig. 4d). The crustal thickening in the weakest model is limited by gravitational forces in the crust that resist lateral gradients in buoyancy. This is also why a topographic high is not created in the weakest model; the crust is too weak to sustain a deflection of its upper boundary. In contrast, with an intermediate viscosity, the crust is weak enough to be deformed and thickened, but strong enough to sustain a topographic high as the crust thickens.

These three models demonstrate three distinct surface expressions associated with root removal, depending on the crustal viscosity (Fig. 4a). They are compatible with the analysis of Neil & Houseman (1999) who highlight the role of crustal deformation and thickening in modulating the topographic response to the gravitational removal of the lithosphere. In the next two models, we consider the effect of vertical stratification of crustal viscosity.

3.2.2 Mid-crustal channel (Model B)

In Model B, the presence of a weak mid-crustal channel is examined. This represents a crust that is relatively hot and is comprised of a weak, felsic upper-mid crust and a strong, mafic lower crust (Fig. 1c). In the model, a 10 km thick layer with a viscosity of 10^{18} Pa s is placed at 30–40 km depth (Fig. 7). Other parameters are identical to those in Model A.

As in Model A, the root is gravitationally unstable and founders as a drip within ∼22 Myr (Fig. 7c). The foundering process is generally the same as that in Model A. However, the surface response to

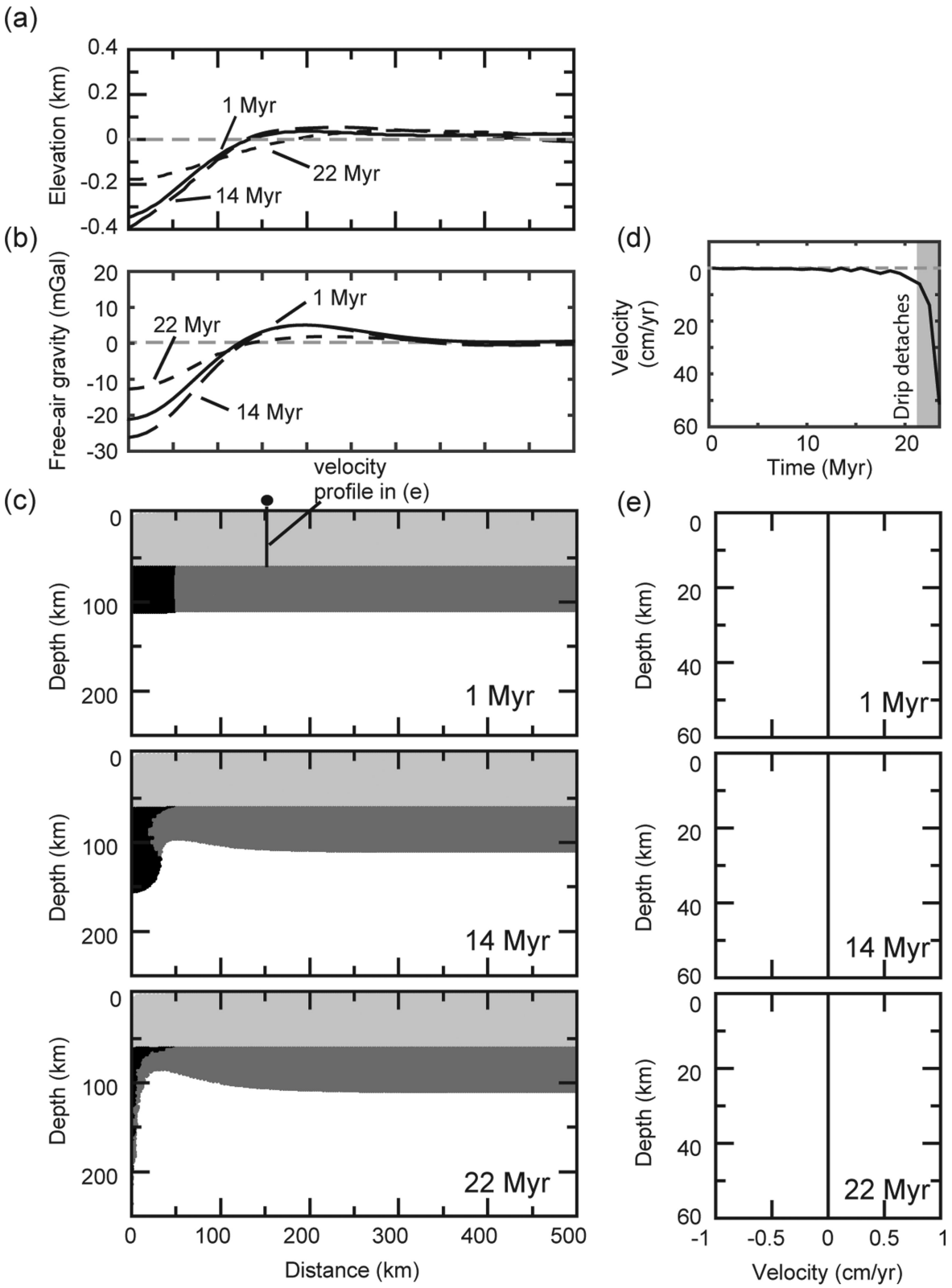

Figure 3. Evolution of Model A, which has a uniformly strong crust with a viscosity of 10^{23} Pa s. (a) Surface topography. (b) Free-air gravity. (c) Model geometry at the given times after the start of phase 2 of the model run. (d) Downward velocity at the base of sinking lithosphere at $x = 0$ km until the drip reaches the lower boundary of model domain. Grey shading denotes when the drip has detached from the lithosphere. (e) Profile of the horizontal crustal flow velocity at $x = 200$ km.

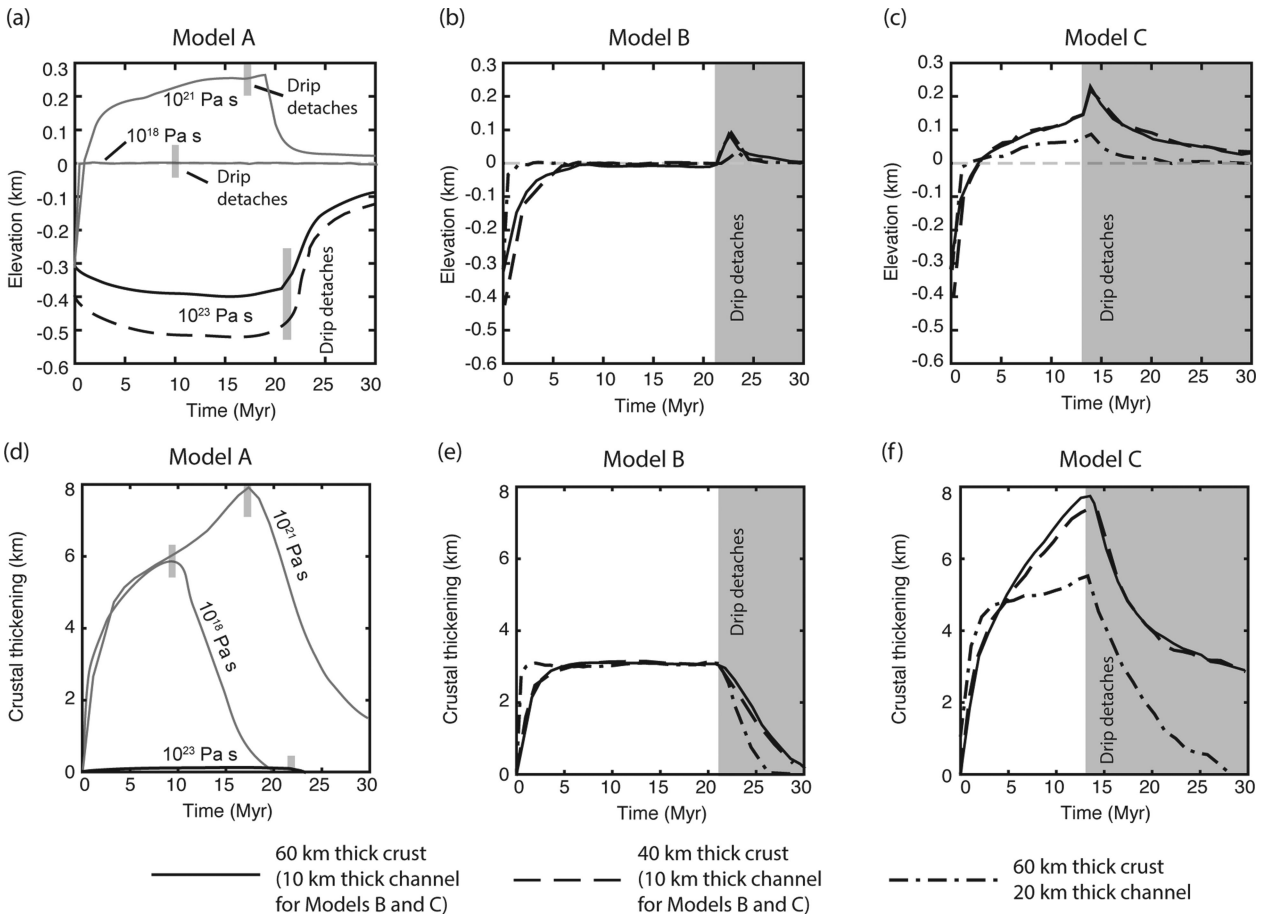

Figure 4. The evolution of surface elevation above the centre of drip ($x = 0$ km) in (a) Model A with crustal viscosity of 10^{23} Pa s (black line), and two models with constant crustal viscosity of 10^{21} and 10^{18} Pa s (grey lines). (b) Model B with a weak mid-crust channel, and (c) Model C with a weak lower-crust channel. (d)–(f) show the evolution of crustal thickening above the centre of the drip for Models A, B and C, respectively. Solid lines are models with 60 km thick crust. Dashed lines are models with 40 km thick crust. Dash–dotted lines are models with 60 km thick crust and 20 km thick weak channel.

removal in this model is quite different. As the root founders, the overlying surface undergoes uplift (Figs 4b and 7a). The surface elevation above the root centre is 0 km by 6 Myr and remains at this elevation until 22 Myr when the root detaches. After the root detaches, the surface uplifts to ∼0.1 km above surroundings and then subsides.

The distribution of stress and deformation in Model B is also distinct from that in Model A (Fig. 6c). The weak mid-crustal channel decouples the mantle root and shallower crust. With the weak channel, the stresses from the dense root are not efficiently transferred to the shallow crust, leading to near-surface stresses of 10^5–10^6 Pa. High deformation and strain rates are localized in the mid-crustal channel with a magnitude of 10^{-15}–10^{-13} s^{-1} over a width of ∼250 km. The detailed crustal deformation is shown in Fig. 7(e). It can be divided into three stages. (1) As the root starts to founder, flow occurs within the mid-crustal channel toward the basin centre. This gradually decreases to 0 cm yr^{-1} by 6 Myr. During this period, the crust beneath the basin centre thickens by ∼3 km (Fig. 4e). It is this crustal thickening that leads to surface uplift, despite the presence of the dense root. (2) Between 6 and 22 Myr, the crustal flow stops (0 cm yr^{-1}) and the crustal thickness does not change. This is associated with a constant surface elevation of 0 km, despite the active downwelling of the root. (3) As the root detaches at 22 Myr, the weak mid-crust flows outward from the basin region and the crust thins to its initial thickness. This corresponds to surface uplift as the dense root is removed, followed by subsidence as the crust thins.

These dynamics are also reflected in the free-air gravity (Fig. 7b). Initially, a negative gravity anomaly is found above the root. As the root detaches, the anomaly is rapidly reduced and throughout the model evolution, the free-air gravity shows little anomaly (<5 mGal). This is because the surface topography is close to zero, and the thickening of the low-density crust is partially balanced by the presence of the dense root.

3.2.3 Lower-crustal channel (Model C)

Model C examines the effect of a lower-crustal channel. A channel with a viscosity of 10^{18} Pa s is placed in the lower 10 km of the crust, in direct contact with mantle lithosphere. This could occur when the deep crust is either moderately hot and felsic or very hot and mafic (Fig. 1d). Other parameters are the same as those in Model A.

Fig. 8 shows that the dense root is removed as a drip that detaches at ∼13 Myr. The earlier detachment time compared to Models A and B is due to the reduced coupling between the root and weak lower crust in this model. Similar to Model B, the weak lower-crustal channel decouples the stress between the mantle root and shallow crust. The near-surface stresses above the root are 10^5–10^6 Pa (Fig. 6d). Deformation localizes in the lower-crust channel, resulting in a strain rate greater than $\sim 10^{-16}$ s^{-1} over a width of 500 km,

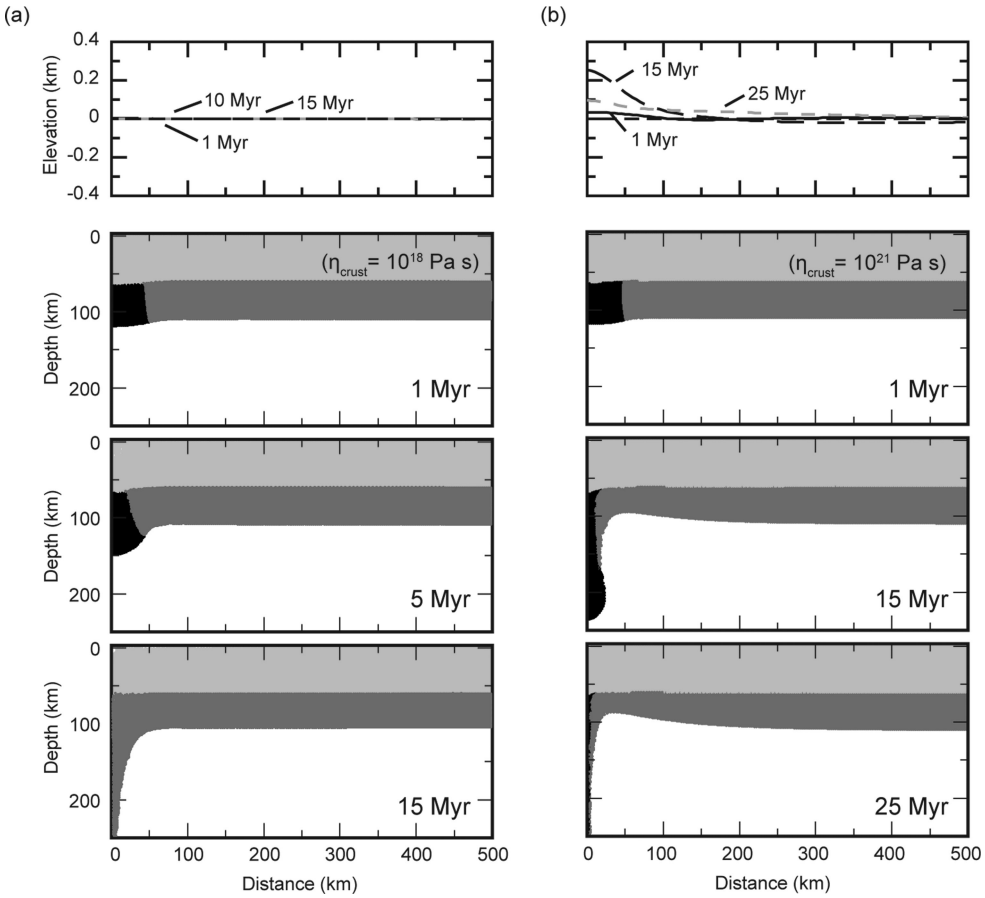

Figure 5. Evolution of models with constant crustal viscosity of (a) 10^{18} and (b) 10^{21} Pa s. The upper plot is surface topography. The lower plots are the model geometry at the given times after the start of phase 2 of the model run.

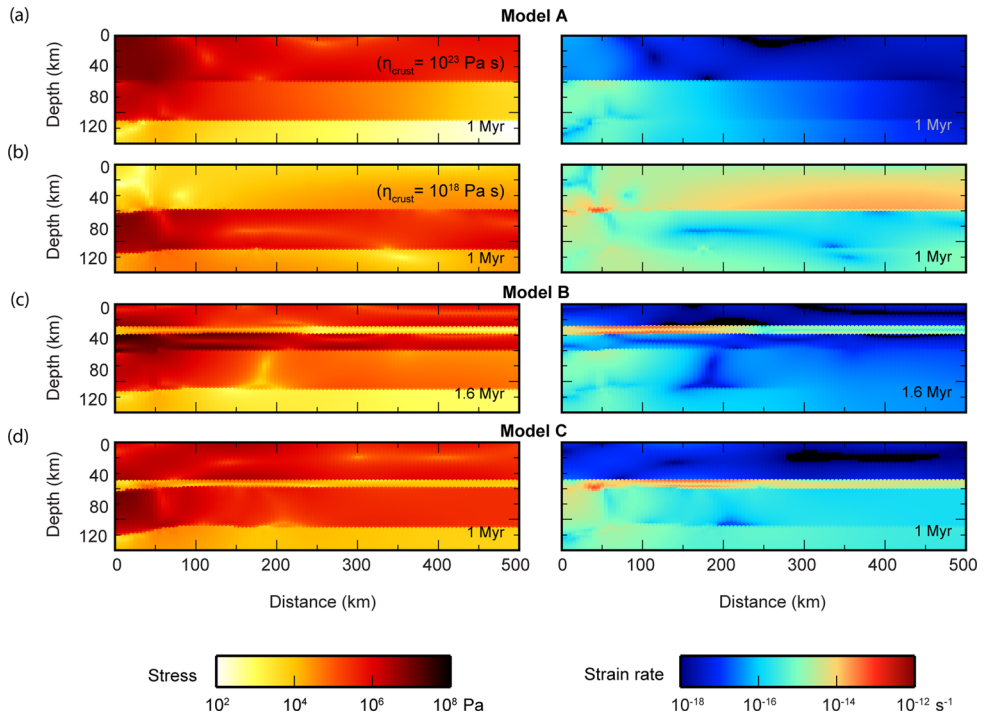

Figure 6. Square root of the second invariant of deviatoric stress and strain rate for (a) Model A with a crustal viscosity of 10^{23} Pa s, (b) a model with crustal viscosity of 10^{18} Pa s, (c) Model B with a weak mid-crustal channel and (d) Model C with a weak lower-crustal channel.

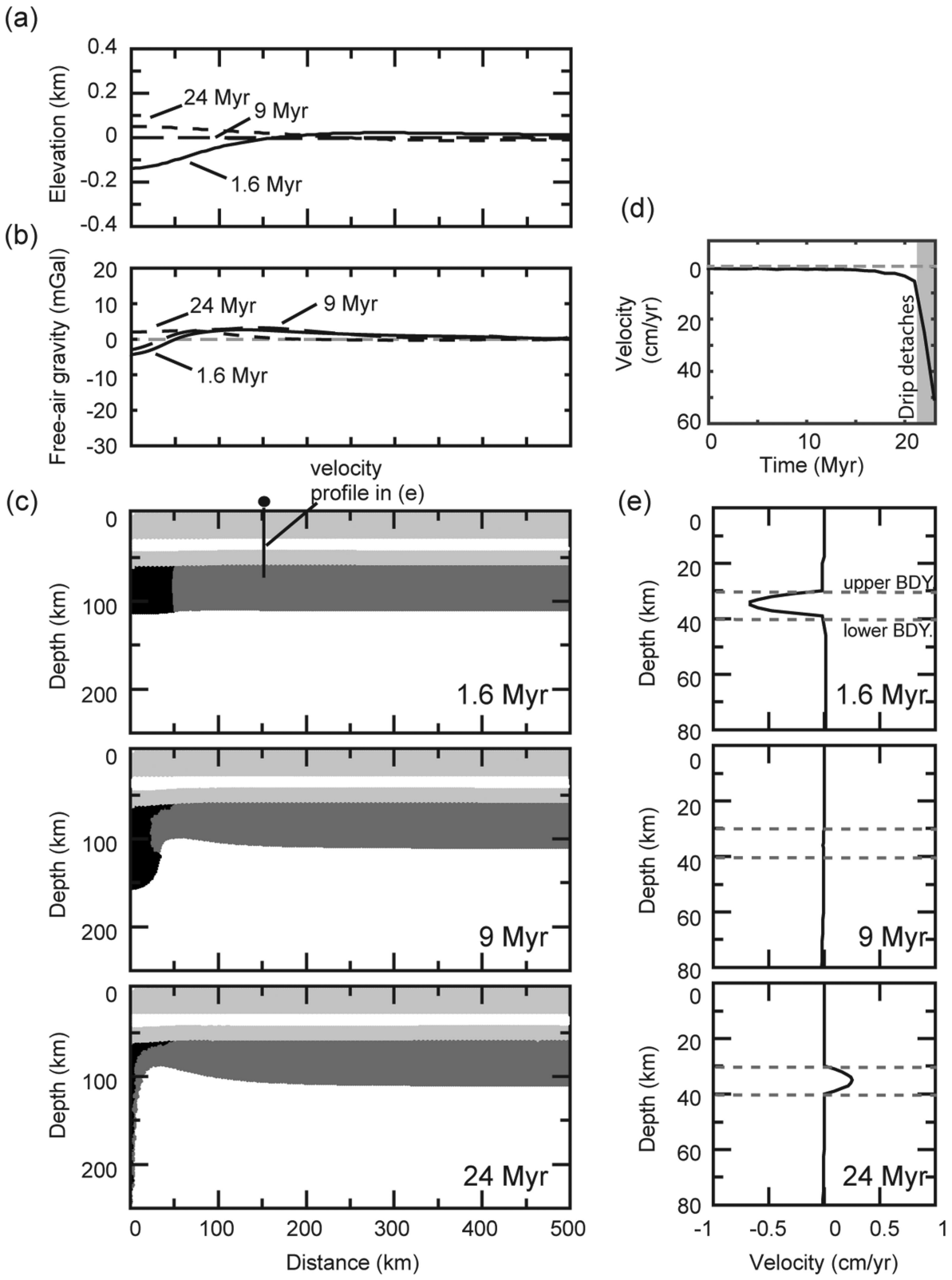

Figure 7. Evolution of Model B, with a weak mid-crustal channel (light grey region in crust). (a) Surface topography. (b) Free-air gravity. (c) Model geometry. (d) Downward velocity at the base of the drip at $x = 0$ km. The grey shading denotes when the drip has detached from the lithosphere. (e) Profile of the horizontal crustal flow velocity at $x = 200$ km. Dashed lines show the channel boundaries. BDY = boundary.

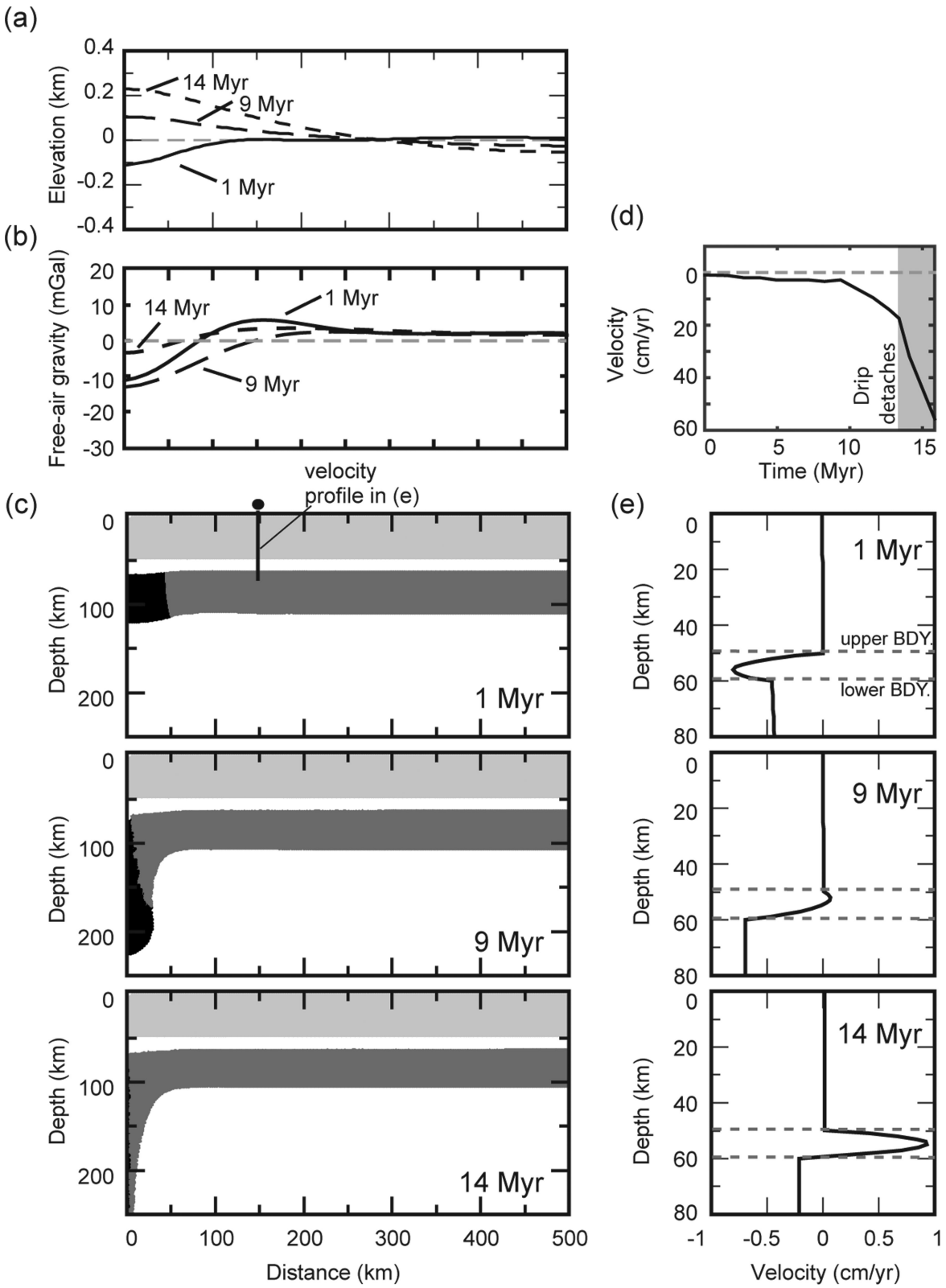

Figure 8. Evolution of Model C, with a weak lower-crustal channel (light grey region in crust). (a) Surface topography. (b) Free-air gravity. (c) Model geometry. (d) Downward velocity at the base of the drip at $x = 0$ km. The grey shading denotes when the drip has detached from the lithosphere. (e) Profile of the horizontal crustal flow velocity at $x = 200$ km. Dashed lines show the channel boundaries. BDY = boundary.

with the highest deformation rate (10^{-15}–10^{-13} s^{-1}) located in a 250 km wide region above the drip. The higher deformation rate in this model compared to Model B is because the weak channel is in direct contact with the mobile mantle, and thus experiences greater shearing (see Section 4).

The evolution of surface topography (Figs 4c and 8a) and crustal deformation (Figs 4f and 8e) can be divided into three stages. (1) In the first 3 Myr, the surface uplifts to 0 km. This is accompanied by flow of the entire weak lower crust towards the root region and crustal thickening by ∼3 km. (2) Between 3 and 13 Myr, crustal deformation continues, resulting in further crustal thickening and surface uplift. In the lower-crust channel, the upper part flows outward from the root region, while the lower part still moves toward the root. At the time of root detachment (13 Myr), the crust has thickened by nearly 8 km and the surface is ∼0.14 km above its surroundings. (3) After the root detaches, the surface exhibits uplift, followed by subsidence as the thickened crust starts to deflate through outward crustal flow.

The crustal thickening induced by the foundering root also affects the free-air gravity (Fig. 8b). Over the centre of the root, the gravity anomaly remains negative throughout the removal process, despite the surface uplift. This is because crustal thickening causes low-density crust to displace the mantle and this has a greater effect on the gravity field than the formation of the topographic high. In this model, the topography and free-air gravity anomalies above the root have opposite signs during root removal, whereas they have the same sign in Models A and B.

Note that after the root detaches, Model C has a thick lithosphere in the vicinity of the root (Fig. 8c). This is due to the weak lower crust which allows a greater area of lithosphere to be entrained by the drip; the velocities profiles show that the mantle lithosphere at the edge of the basin has a non-zero velocity (Fig. 8e). In contrast, Models A and B exhibit lithospheric thinning following drip removal (Figs 3c and 7c). In these models, lower crust is strong enough to resist horizontal deformation (Figs 3e and 7e), and this restricts the amount of mantle lithosphere that is carried laterally.

4 ANALYTICAL CALCULATION OF CRUSTAL FLOW

Section 3 shows the dynamics of lithosphere removal for end-member crustal viscosity structures. In Model A, the entire crust is too strong to deform, and root foundering is accompanied by surface subsidence. In contrast, the presence of a weak crustal layer in Models B and C allows for crustal deformation and surface uplift prior to root detachment. In this section, we analyse the origin of crustal deformation and the varying topographic responses.

4.1 Mid-crustal channel model

We first consider the evolution of Model B, in which root foundering is accompanied by crustal thickening and a relatively flat topography (Fig. 7). This behaviour can be analysed in terms of a pressure/gravitationally driven channel flow within the weak mid-crust (*cf.* Kruse *et al*. 1991). The presence of the dense root initially causes surface subsidence, which induces low pressures in the overlying crust relative to the adjacent regions. This triggers flow within the weak channel toward the low pressure region and leading to crustal thickening and surface uplift above the root. As shown in Appendix A, analytic equations can be used to relate the lateral pressure gradient and flow velocities. In this case, the mid-crustal channel is bounded by strong upper and lower boundaries that cannot be deformed laterally. All flow is confined to the weak channel, and the velocity profile (Fig. 7e) corresponds to that of Poiseuille flow, in which the flow is symmetric about the centre of the channel and velocity decreases to zero at the upper and lower boundaries (Turcotte & Schubert 2002). The average flow velocity in the channel ($\bar{v}$) is related to the lateral gradient in surface topography:

$$\bar{v} = \frac{{h_{\rm ch}}^2}{12\eta_{\rm ch}}\rho_c g \frac{S}{L_{\rm basin}} \tag{1}$$

where $h_{\rm ch}$ and $\eta_{\rm ch}$ are the thickness and viscosity of the ductile channel, ρ_c is the crustal density, g is the gravitational acceleration, S is the surface elevation at the basin centre ($x = 0$ km) and $L_{\rm basin}$ is the half-width of basin. In the coordinate system of our models, a negative S corresponds to a basin above the root region; at this time, $\bar{v}$ is also negative, meaning that the crustal flow is towards the root.

Eq. (1) predicts a linear relationship between the average channel flow velocity and the surface deflection. Fig. 9(a) shows the evolution of observed surface deflection and average flow velocity at the basin edge for Model B, as well as the expected relationship based on eq. (1). The modeling result is in good agreement with the theoretical prediction, with a root mean square (rms) difference of 0.07 cm yr^{-1}, showing that the observed mid-crustal channel flow is consistent with a pressure-driven flow.

Eq. (1) also shows that the channel flow ceases when surface is flat ($S = 0$). The channel flow can only thicken the crust until it fully balances the surface subsidence caused by the dense root; it is impossible to create a topographic high above the dense root. If channel flow is rapid, the surface can uplift so that there is flat topography ($S = 0$) before the root detaches and mid-crustal channel flow stops. In Model B, this occurs between 6 and 20 Myr (Figs 4b and 7e).

4.2 Lower-crustal channel

Gravitational lithosphere removal in Model C produces a short-lived basin at the surface, followed by uplift to a topographic high (Fig. 8). This is related to lateral flow in the weak lower-crustal channel that leads to crustal thickening above the dense root. Flow arises from a combination of pressure-driven Poiseuille flow associated with topographic variations created by the dense root and Couette flow created by basal shearing by the underlying mantle, as the channel is in contact with the mobile mantle (Turcotte & Schubert 2002). As a result of basal shearing, the velocity at the base of the channel is not zero, and flow velocities are asymmetric about the centre of the channel (Fig. 8e). This leads to an average flow velocity in the channel ($\bar{v}$) of:

$$\bar{v} = \frac{{h_{\rm ch}}^2}{12\eta_{\rm ch}}\rho_c g \frac{S}{L_{\rm basin}} + \frac{1}{2}v_0 \tag{2}$$

where v_0 is the horizontal velocity at the lower boundary of the channel. The first term corresponds to topographically driven flow, and the second term corresponds to the average Couette flow in the channel (see Appendix A for details).

For a given basal velocity (v_0), this equation predicts a linear relationship between the surface deflection and average crustal flow velocity. Fig. 9(b) shows the observed surface deflection and channel velocity for Model C. The poor linear relationship is due the fact that the basal velocity of the channel increases over time (Fig. 9c), as root detachment is non-linear (*cf.* Houseman & Molnar 1997). In Fig. 9(d), the component of Poiseuille flow at each time is isolated from the observations (Fig. 9b) by subtracting half of the lower boundary

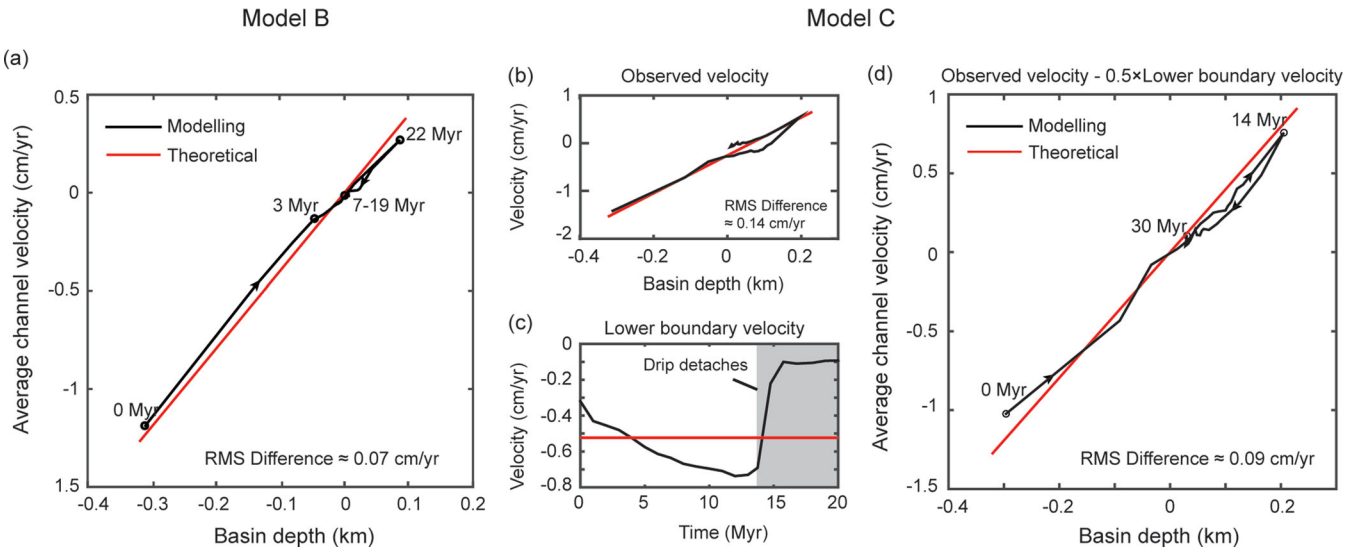

Figure 9. Comparison of observed and theoretical crustal channel flow. (a) Relationship between the average velocity at $x = 200$ km in the mid-crust channel and the surface elevation above the centre of drip. The black line is the modelling result (Model B) and the red line is the theoretical prediction based on the model parameters (eq. 1). Root mean square (rms) difference is ~0.07 cm yr^{-1}. (b) Relationship between the average velocity at $x = 200$ km in the lower-crustal channel and the surface elevation above the centre of the drip. The black line is the modelling result (Model C) and the red line is the theoretical prediction (eq. 2). In the theoretical prediction, v_0 is the average horizontal velocity of the lower boundary of the weak channel [red line in (c)]. (c) The horizontal velocity of the lower boundary of the weak channel in Model C over time. (d) Relationship between the surface elevation above the drip and the Poiseuille flow in the channel (black line). This is calculated by subtracting half of the lower boundary velocity [black line in (c)] from the observed average channel velocity [black line in (b)] at each time. The red line is the theoretical prediction for Poiseuille flow based on the model parameters (eq. 1). The rms difference is ~0.09 cm yr^{-1}.

velocity at that time (black line in Fig. 9c). With this, there is a clear linear relationship between the surface deflection and flow velocity and this agrees well with the expected value from eq. (2) without the basal velocity (v_0) component (rms error of 0.09 cm yr^{-1}). This demonstrates that the channel flow in the lower crust is driven by both lateral pressure variations and basal shearing.

With a lower-crustal channel, the surface can form a topographic high above the foundering root (Fig. 4c). The Poiseuille flow is driven by the surface deflection, which can only uplift the surface above the root to its initial elevation (eq. 1). However, the Couette flow is induced by shear from the descending root, which can lead to enhanced crustal thickening (Pysklywec & Shahnas 2003). Couette flow provides the additional force to elevate the topography above surrounding areas. From eq. (2), the channel will have an average velocity ($\bar{v}$) of 0 when the surface elevation is:

$$S = -6\frac{\eta_{ch}}{{h_{ch}}^2}\frac{L_{basin}}{\rho_c g}v_0 \qquad (3)$$

where the surface deflection (S) has a positive sign because v_0 is negative in the coordinate system of our models. A positive S indicates a topographic high above the root. At this time, the Couette flow contribution (which is always directed toward the root) is balanced by the Poiseuille flow that is directed outward from the topographic high. Eq. (3) therefore shows the maximum elevation that can be created above the dense root. Once the dense root detaches, v_0 goes to zero and the topographic high relaxes (Fig. 4c).

5 PARAMETER VARIATIONS

Models B and C represent end-member cases of a strong crust with a 10 km thick, extremely weak (viscosity of 10^{18} Pa s) channel. As the dense root sinks, channel flow is readily induced within the weak channel, resulting in rapid crustal thickening and uplift prior to root detachment. In this section, we examine how variations in the properties of the root and overlying crust affect the crustal thickness and topography.

5.1 Root density and channel viscosity

We first vary the channel viscosity and root density. Both mid-crustal and lower-crustal channels are considered, each with a 10 km channel thickness. We test a suite of numerical models with crustal channel viscosities of 10^{18}–10^{21} Pa s, and root densities that are 20–240 kg m^{-3} greater than that of underlying mantle (Table 1). These ranges are consistent with observations of crustal channel viscosity (Section 2) and the density of mantle lithosphere materials (e.g. Jull & Kelemen 2001).

5.1.1 Mid-crustal channel

Fig. 10 shows the model results for a mid-crustal channel. These plots show the surface elevation above the dense root (z_0) at the start of phase 2 (Fig. 10a), the surface elevation at the time of root detachment (z_d) (Fig. 10b), the uplift ratio (defined as $|z_d - z_0|/|z_0|$; an uplift ratio of 100 per cent corresponds to full recovery of the initial subsidence, Fig. 10c), and the amount of crustal thickening above the root at the time of root detachment (Fig. 10d).

In all models, the surface is initially a topographic low due to the presence of the dense root, with greater subsidence for a denser root (Fig. 10a). As the root founders, the magnitudes of surface uplift (Figs 10b and c) and crustal thickening (Fig. 10d) depend on the relative rates of root detachment time and channel flow. In these models, the detachment time is primarily controlled by the root density, as the viscosity of the lower crust and mantle are not varied. A more dense root has an earlier detachment time, and therefore there is a shorter time for crustal flow. Channel flow also depends on root density, as well as the channel viscosity; flow rates increase for both a higher root density, owing to the larger lateral

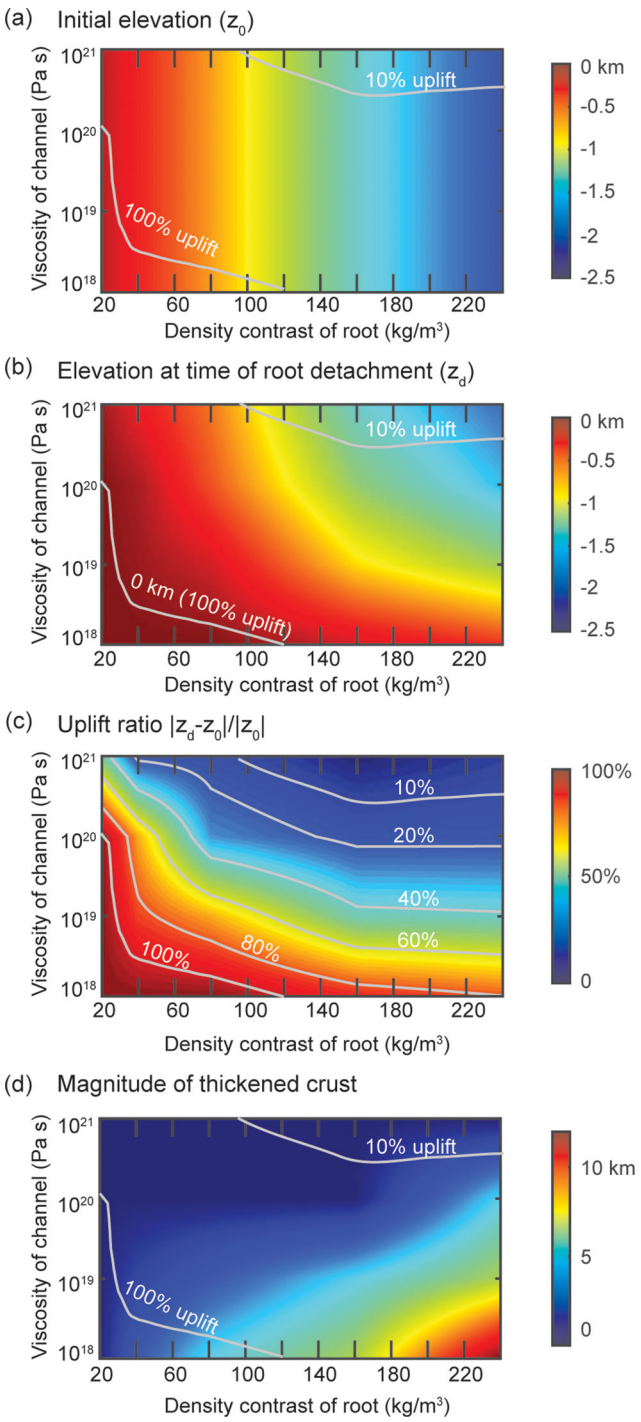

Figure 10. Effect of variations in mid-crustal channel viscosity and root density on: (a) the surface elevation above the centre of the drip (at $x = 0$ km) at the start of phase 2 (z_0; negative values indicate subsidence), (b) the surface elevation above the centre of the drip at the time of root detachment (z_d), (c) the surface uplift ratio ($|z_d - z_0|/|z_0|$) and (d) the magnitude of crustal thickening above the centre of the root at the time of root detachment.

pressure gradient created by the initial subsidence, and a lower channel viscosity (eq. 1).

Three main surface responses are observed. (1) The surface remains as a topographic low throughout root removal, with an uplift ratio of less than 10 per cent. This happens when the channel viscosity is high (5×10^{20} Pa s or greater) and the root is dense (>100 kg m^{-3} denser than mantle). The flow velocity is relatively small in the high-viscosity channel, and the root detaches fairly rapidly. Therefore, the induced channel flow results in only minor crustal thickening and surface uplift over the timescale of root detachment. (2) The basin undergoes nearly 100 per cent uplift prior to root detachment. In this case, the channel has a low viscosity ($<10^{20}$ Pa s) and the root is moderately dense (<120 kg m^{-3} denser than the mantle). The low viscosity allows for rapid channel flow that thickens the crust and uplifts the surface over the detachment timescale. (3) Between the above cases, an intermediate response is observed where there is partial basin uplift (uplift ratio is between 10 and 100 per cent) before root detachment. The crust thickens in this case, but it is not sufficient to create full-basin uplift because the crustal flow rate is sluggish within a high-viscosity channel and/or the root density causes rapid detachment.

5.1.2 *Lower-crustal channel*

Fig. 11 shows the model results for a lower-crustal channel. In this case, the time of root detachment is affected by root density and lower-crustal viscosity. A denser root and/or weaker lower crust lead to both faster root removal and more rapid channel flow. Again, all models start with a topographic low above the root (Fig. 11a). The later behaviour can be divided into three styles: (1) models that demonstrate negligible surface uplift as the dense root is removed (uplift ratio < 10 per cent). This occurs in models with a high channel viscosity (7×10^{20} Pa s or greater) and a high root density (>120 kg m^{-3} denser than mantle). In these models, root detachment occurs too rapidly for flow within the high-viscosity channel to significantly thicken the crust. (2) Full uplift of the basin during root removal (uplift ratio of 100 per cent or greater). The greatest uplift is observed where the root density is relatively low (<40 kg m^{-3} greater than mantle density) and the channel viscosity is 10^{19}–10^{20} Pa s, and in these cases, the surface above the root is a topographic high (i.e. positive surface elevation) at the time of detachment. Here, the root detachment time is long enough to allow for sufficient channel flow to thicken the crust and create high topography; at lower viscosities, the root detachment time is too small and at higher viscosity, the channel flow is too sluggish. (3) An intermediate case of moderate uplift during root removal (uplift ratio of 10−100 per cent). The crustal thickening is not sufficient for full surface uplift before root detachment. This occurs because the flow velocity is relatively slow in a high-viscosity channel and/or the root detachment occurs quickly due to a high root density or low-viscosity lower crust. Note that the viscosity of mantle lithosphere is 10^{21} Pa s in our models. The crustal thickening induced by the shear stress at the base of crust is more significant when the viscosity contrast at interface between crust and mantle is small (Neil & Houseman 1999; Molnar & Houseman 2013, 2015). Therefore, the crust thickens most when the channel viscosity is $\sim 10^{20}$ (Fig. 11d).

Overall, the magnitude of crustal thickening and syn-removal uplift are greater than in mid-crustal channel models. For a lower-crust channel, a greater range of conditions create 100 per cent uplift. In addition, a positive surface elevation prior to root detachment only occurs in the lower-crustal channel models. These differences are due to the fact that lower-crustal flow is driven by both the crustal lateral pressure gradient and basal shearing (eq. 2), resulting in more rapid channel flow; mid-crustal flow is driven only by the pressure gradient.

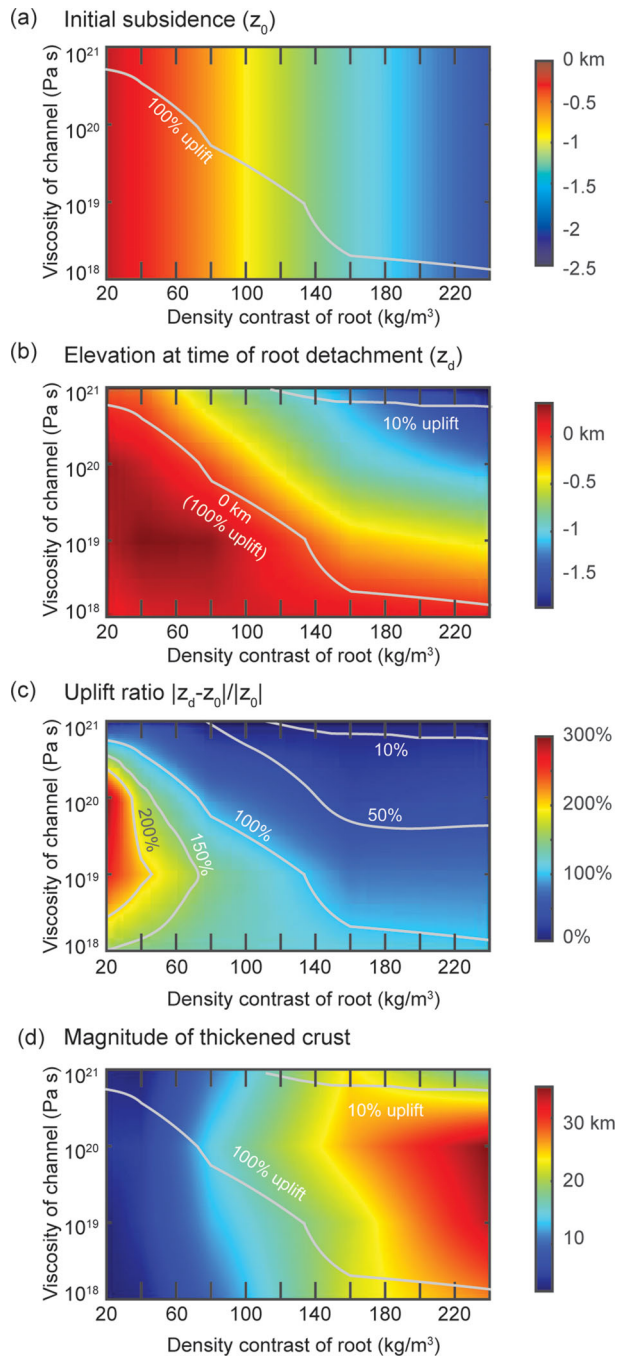

Figure 11. Effect of variations in lower-crustal channel viscosity and root density on: (a) the surface elevation above the centre of the drip at the start of phase 2 (z_0; negative values indicate subsidence), (b) the surface elevation above the centre of the drip at the time of root detachment (z_d), (c) the surface uplift ratio ($|z_d-z_0|/|z_0|$), and (d) the magnitude of crustal thickening above the centre of the root at the time of root detachment.

5.2 Crustal and channel thickness

We also consider how the surface response to lithosphere removal is affected if the crust is thinner or the channel is thicker than assumed in the previous models. First, Models A, B and C are rerun with a 40 km crust (Table 1), comparable to the average thickness of continental crust. The channel properties (thickness of 10 km and viscosity of 10^{18} Pa s) are identical to those in Models B and C. The evolution of surface elevation and crustal thickness above the root are shown in Fig. 4 (dashed lines). In all cases, the initial surface subsidence in phase 1 is greater than for the original models, creating a deeper, narrower basin. This is because with a thinner crust, the density anomaly is closer to the surface and the thinner crust has less viscous resistance. However, the later evolution is similar to the original models. Model A exhibits uplift at the time of root detachment, and Models B and C exhibit crustal channel flow during root foundering, resulting in surface uplift prior to detachment. The surface response and crustal thickening are not strongly affected by the initial crustal thickness.

We test the effects of channel thickness by introducing a 20 km thick channel to the mid-crust and lower crust in Models B and C, respectively (60 km thick crust and channel viscosity of 10^{18} Pa s); the lower boundary of the channel is at the same depth as in the original models (Table 1). A thicker weak channel may form in regions with higher heat flow (Fig. 1). Fig. 4 (dash–dotted lines) shows that the crustal thickness above the root increases more rapidly, resulting in higher surface uplift rates and earlier basin uplift compared to models with a 10 km thick channel (solid lines). This is because the Poiseuille flow velocity increases in a thicker channel (eq. 1). In the model with a lower-crustal channel, when the surface above the root becomes a topographic high, outward Poiseuille flow is produced in the channel, as this region now has high pressure compared to the adjacent crust. The magnitude of this flow is larger for a thicker channel. As a result, the maximum elevation (Fig. 4c) and crustal thickening (Fig. 4f) are reduced relative to those in Model C. This is consistent with eq. (3) in which the maximum surface elevation is inversely proportional to the squared channel thickness. Therefore, a thicker channel limits the growth of high topography.

6 DISCUSSION

6.1 Surface observables of mantle dynamics

Topography on the Earth's surface reflects the combination of static effects (i.e. lateral variations in lithosphere density) and dynamical processes within the lithosphere and underlying mantle (e.g. Braun 2010; Flament *et al*. 2013). In this study, we have focused on the temporal evolution of surface topography during gravitational lithosphere removal. Removal is initiated by introducing a high-density block in the mantle lithosphere, which induces a downward stress on the overlying material. The key result is that the presence of a weak, low-density crustal layer can significantly modify the surface expression of removal. If the crust is stronger than the mantle (e.g. Model A; Fig. 3), the mantle stresses are efficiently transferred to the surface; there is little to no crustal thickening and removal is accompanied by surface subsidence. Conversely, if there is a weak layer within the mid-crust (e.g. Model B; Fig. 7) or lower crust (e.g. Model C; Fig. 8), mantle stresses induce deformation of this layer, resulting in crustal thickening and syn-removal uplift of the surface. These results are compatible with earlier studies that investigate the dynamics of weak crust above foundering mantle lithosphere (e.g. Neil & Houseman 1999; Pysklywec & Shahnas 2003; Pysklywec & Beaumont 2004; Elkins-Tanton 2007; Molnar & Houseman 2013; Wang *et al*. 2014; Molnar & Houseman 2015; Wang *et al*. 2015).

Our models use a purposefully simple layered rheological structure to demonstrate the time-dependent nature of crustal deformation during lithosphere removal. The models show that two factors contribute to the induced crustal deformation. First, the downwelling mantle creates a low pressure in the overlying crust, as the presence of the dense root causes an initial surface

subsidence. The resulting lateral pressure gradient induces Poiseuille flow within a weak crustal layer, leading to crustal thickening above the area of downwelling. This is similar to crustal channel flow driven by lateral topographic variations on the Earth's surface (e.g. Kruse *et al*. 1991; McQuarrie & Chase 2000; Beaumont *et al*. 2001, 2006; Grujic 2006). Second, crustal deformation arises from shearing of the deep crust by the underlying mantle (e.g. Pysklywec & Shahnas 2003). This requires that the weak crustal layer is in contact with the mobile mantle. Shearing creates Couette flow within the weak channel and allows further thickening of the crust above the downwelling root.

The magnitude of crustal thickening depends on the location and properties of the weak crustal channel, as well as the timescale of lithosphere removal, which is primarily controlled by the density and viscosity of the dense root in our models. Where the channel is thick and/or weak, crustal flow may be significant over the timescale of root removal, resulting in greater crustal thickening and surface uplift. If the weak channel is in contact with the mobile mantle (e.g. a lower-crustal layer), deformation is driven by both the lateral pressure gradient and basal shearing, and this can create a topographic high and a negative free-air gravity anomaly above the foundering lithosphere. This shows that even though the mantle stresses produce a negative dynamic topography, the surface elevation can still be positive. If the weak channel is isolated from the mobile mantle (e.g. a mid-crustal layer), crustal thickening occurs only through pressure-driven flow, resulting in a (partial) recovery of the original surface subsidence, but the mantle stresses do not generate high topography or a strong gravity anomaly.

We note that our models use a simplified approach to demonstrate the fundamental physical mechanisms for crustal deformation induced by mantle stresses. For example, our models assume the instantaneous emplacement of a dense lithospheric root, and we focus on the effects of its gravitational removal. In reality, lithosphere removal may be induced by a perturbation to the cool, dense mantle lithosphere (e.g. Houseman *et al*. 1981) or by the gradual growth of a dense assemblage (Wang *et al*. 2015, and references therein).

In addition, the models assume constant viscosity and density within each of the layers. Density should vary with temperature, which will affect the buoyancy forces with the crust and mantle and the resulting dynamics and topographic deflection. More importantly, laboratory deformation experiments show that crust and mantle rocks follow a non-Newtonian, temperature-dependent rheology (e.g. Gleason & Tullis 1995; Ranalli 1995; Mackwell *et al*. 1998). As a result, the effective viscosity of the crust varies with temperature, strain rate, and possibly pressure. Studies that consider a Newtonian crust with a viscosity that decreases with increasing depth (temperature) show that topographic uplift decreases as the viscosity variation in the crust increases (Elkins-Tanton 2007; Molnar & Houseman 2015). Only the lowermost crust is able to flow, which limits the amount of thickening and uplift. The viscosity ratio at the crust–mantle boundary is important, with the greater thickening and surface uplift where the crust and mantle viscosities are similar (Molnar & Houseman 2015). This is likely because the crust experiences greater shearing by the underlying mantle. A non-Newtonian rheology may enhance the formation of localized, weak channels in the crust, but to date there have been no systematic studies of lithosphere removal for a non-Newtonian crust. Our earlier models that include a non-Newtonian rheology demonstrate that crustal thickening and surface uplift can occur above a region of lithosphere removal (Wang *et al*. 2014, 2015).

We also note that our models do not include elastic or frictional plastic (brittle) rheologies. Elastic or brittle deformation can induce surface deflections at shorter wavelengths (Buiter *et al*. 2002; Burov & Guillou-Frottier 2005; Burov & Cloetingh 2009; Duretz *et al*. 2012; Cloetingh *et al*. 2013; François *et al*. 2013). Models that include a elastic-viscous-plastic rheology suggest that the integrated strength becomes laterally variable in the shallow crust (e.g. Burov & Guillou-Frottier 2005; Burov & Cloetingh 2009). This leads to a localization of deformation and small-scale surface deflection over length scales of 1's–10's of km. This can be enhanced if brittle faulting occurs in regions of the crust where stresses exceed the brittle (frictional-plastic) strength. Our earlier models show that the inclusion of frictional-plastic deformation results in the development of a more localized basin above a downwelling dense root (Wang *et al*. 2015).

Finally, our models are based on 2-D plane-strain calculations, and therefore crust and mantle is confined to the model plane. In 3-D, the distribution of buoyancy forces may be different than in 2-D; in particular, the magnitude of stresses and the surface deflection may be reduced if the dense body is spatially confined. Also, crustal flow can be entrained from all directions and crustal thickening could be more rapid than in a plane-strain model. Therefore, in 3-D, surface uplift may occur under a greater range of conditions than predicted by our 2-D models (Figs 10 and 11). However, the timescale for lithosphere removal in 3-D may be somewhat less, which will reduce the amount of time for crustal thickening and uplift. There have been a few studies that address the dimensional effects using 2-D axisymmetric models (e.g. Hoogenboom & Houseman 2006; Elkins-Tanton 2007) and full 3-D models (e.g. Moresi & Lenardic 1999). These show that downwelling mantle can induce crustal deformation and surface uplift, but further work is needed to better understand the effects of rheological stratification in 3-D.

6.2 Implications for crustal structure

Despite the limitations noted above, our models provide insight into how mantle-based stresses may induce deformation of the overlying crust. We can use the models to draw some general conclusions about the conditions under which crustal deformation may be significant enough to affect the topographic expression of lithospheric removal. As an example, we consider removal of a root that is 120 kg m^{-3} denser than mantle. This density corresponds to a mantle lithosphere root that consists of 48 per cent eclogitized rocks (based on a mafic eclogite density of 3550 kg m^{-3}; Christensen & Mooney 1995). The eclogitized lithosphere roots are proposed to occur in many metamorphic and/or magmatic environments such as the Sierra Nevada and central Andean plateau (e.g. Kay & Kay 1993; Ducea 2001; Saleeby *et al*. 2003, 2012). From Figs 10 (mid-crustal channel) and 11 (lower-crustal channel), we identify the critical channel viscosities needed for an uplift ratio of < 10 per cent (surface remains as a topographic low), an uplift ratio of 10–100 per cent (partial uplift) and an uplift ratio ≥ 100 per cent (full uplift to a topographic high). These viscosities can be compared to the expected viscosities for different crustal compositions (Fig. 12a). As crustal viscosity decreases with increasing temperature, we can then infer the general thermal conditions that allow different surface deflections. We use strain rate of 10^{-14} and 10^{-16} s^{-1} for viscosity profiles in Fig. 12(a); the higher strain rate is comparable to that in the weak channel in the numerical models (Fig. 6) and the lower strain rate is shown for comparison.

For the mid-crustal channel, the removal of a dense root causes subsidence (with less than 10 per cent syn-drip uplift) if the channel viscosity is higher than 7×10^{20} Pa s (Fig. 10). This suggests that

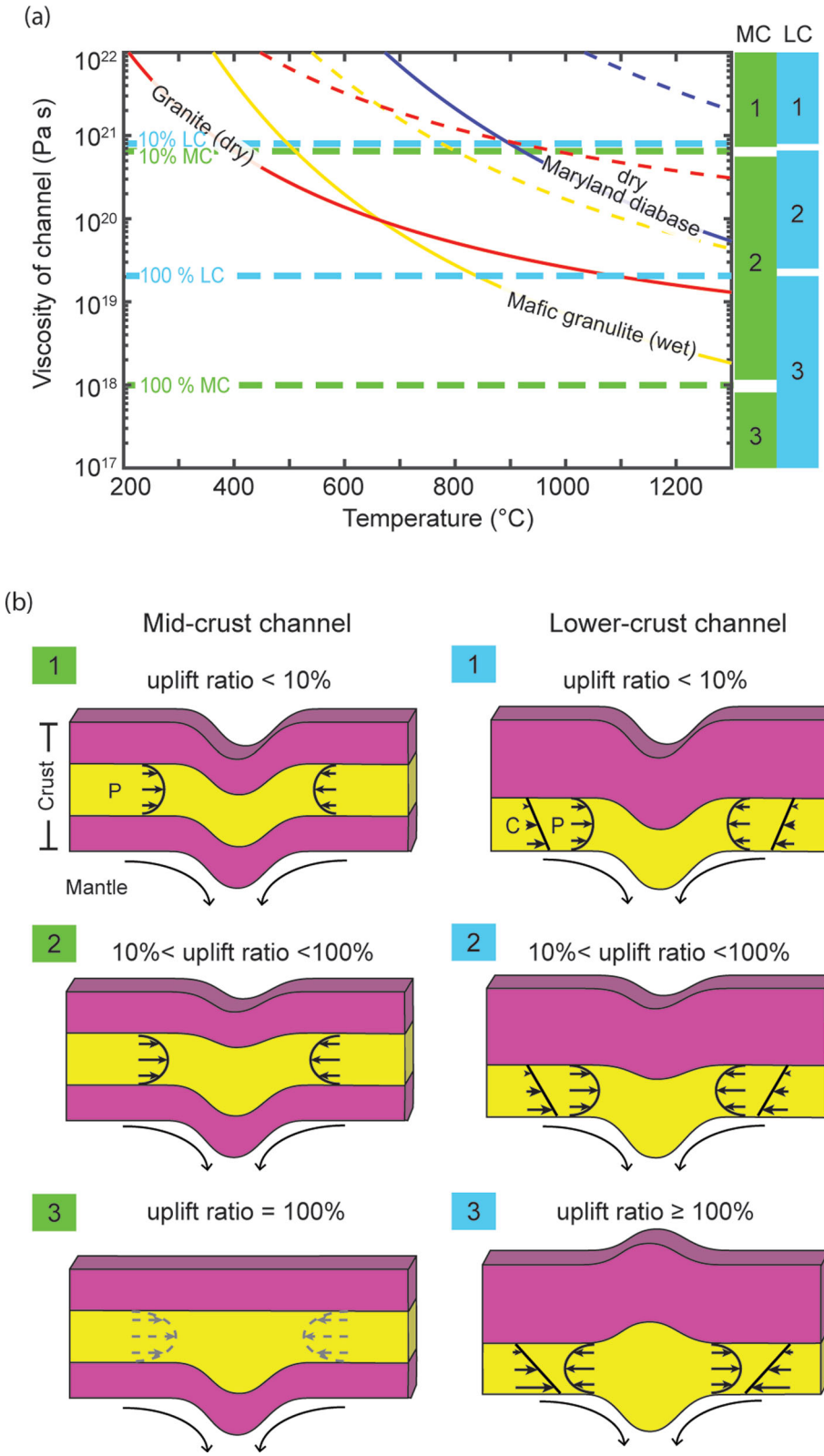

Figure 12. (a) Variation in effective viscosity of different crustal compositions with temperature, based on laboratory-derived rheological parameters of dry granite (Ranalli 1995; red lines), hydrated mafic granulite (Wang *et al*. 2012; yellow lines) and dry Maryland diabase (Mackwell *et al*. 1998; blue lines). These cover a reasonable range of crustal compositions. Calculations use a strain rate of 10^{-14} s^{-1} (solid lines) and 10^{-16} s^{-1} (dashed lines). The higher strain rate is comparable to the strain rate in the weak crustal channel in our numerical models. Horizontal dashed lines are the predicted surface uplift ratios for mid-crust channel models (green lines) and lower-crust channel models (blue lines), derived from Figs 10 and 11 for a root density excess of 120 kg m^{-3}. (b) Schematic plots of crustal flow and surface deflection during gravitational lithosphere removal for different uplift ratios for a mid-crustal channel (left) and lower-crustal channel (right). The weak channel is shown in yellow; strong crust is purple. P = Poiseuille flow and C = Couette flow.

if the mid-crust is dry and felsic or wet and mafic, mid-crustal temperatures should be less than ∼400–500 °C at a strain rate of 10^{-14} s^{-1} (Fig. 12a); temperatures could be higher for a dry and mafic mid-crust or one that deforms at a lower strain rate. On the other hand, a mid-crustal channel with a viscosity between 10^{18} Pa s and 7×10^{20} will allow partial surface uplift during root removal (10–100 per cent uplift ratio). This occurs for temperatures greater than ∼400–500 °C for a dry and felsic or wet and mafic mid-crust. Note that the formation of a mid-crustal channel also requires that the lower crust is too strong to deform (viscosity greater than 10^{21} Pa s). Assuming a strain rate of 10^{-16} s^{-1}, this corresponds to lower-crustal temperatures less than ∼750 °C if the lower crust is wet and mafic. Higher lower-crustal temperatures are possible for a dry, mafic composition or if the strain rate is lower. For a full-surface uplift (100 per cent uplift ratio), the mid-crust viscosity needs to be less than 10^{18} Pa s, which is unlikely for the crustal compositions shown in Fig. 12(a).

For a lower-crust channel which is in contact with the mobile mantle, syn-drip subsidence (uplift less than 10 per cent) requires a lower-crustal viscosity greater than $\sim 8 \times 10^{20}$ Pa s (Fig. 11). For a strain rate of 10^{-14} s^{-1}, this corresponds to temperatures less than ∼900 °C for a dry and mafic composition or ∼400–500 °C for lower crust that is dry and felsic or wet and mafic (Fig. 12a). On the other hand, significant lower-crustal flow, leading to the formation of a topographic high (uplift greater than 100 per cent) occurs if the lower-crustal viscosity is less than $\sim 2 \times 10^{19}$ Pa s. This corresponds to lower-crustal temperatures greater than 800–1000 °C for dry and felsic or wet and mafic compositions with a strain rate of $\sim 10^{-14}$ s^{-1}. At intermediate viscosities and temperatures, lithosphere removal will be accompanied by partial (10–100 per cent) surface uplift.

6.3 Examples of intraplate deformation induced by lithosphere removal

We now extend our model predictions to regions where crustal deformation and/or surface deflection have been proposed to be associated with gravitational lithosphere removal. The analysis above shows that temperature and composition affect the vertical rheological structure of the crust, and in particular, a hot crust is susceptible to contraction and thickening by mantle stresses from below. This can occur both within the interior of continental plates or in regions that are close to an active plate boundary. Examples of crustal deformation that have been linked to lithospheric removal include the Isan orogen in Australia (Pysklywec & Beaumont 2004) and the Arizaro basin the central Andes (DeCelles *et al*. 2015; Wang *et al*. 2015). Another example is the Wallowa Mountains in northern Oregon (Fig. 13a). This area experienced ∼200 m of subsidence from 12 to 10 Ma, and then the surface began to uplift, initially at a relatively low rate (∼0.3 km Myr^{-1}) and more rapidly after 6 Ma (∼0.6 km Myr^{-1}, Hales *et al*. 2005, Fig. 13b). The region reached its present elevation of ∼2 km at 3–4 Ma, and it currently appears as a 'bull's eye' shaped highland (Fig. 13a). Seismic studies show that present-day crust here is 10–15 km thicker than the average crustal thickness (30–40 km) in the surrounding areas (e.g. Gao *et al*. 2011).

This surface uplift history is proposed to be related to the removal of a dense magmatic root (Hales *et al*. 2005; Darold & Humphreys 2013). The two stages of surface uplift and the localized thickened crust in the Wallowa Mountains are consistent with crustal deformation during root removal. Our results suggest the initial slow uplift is likely caused by the crustal flow and thickening during root destabilization, and the latter period of rapid uplift corresponds to detachment of the root. If this is correct, it requires that the flow must have occurred in the lower crust, in order to create a topographic high during the root removal phase. At present, the regional heat flow in this area is relatively high (70–80 mW m^{-2}; Blackwell *et al*. 2011), which suggests temperatures of ∼700–1000 °C in the lower 10 km thick crust (Fig. 13c). By comparison with Fig. 12(a), we conclude that in order to create a topographic high during removal, the lower crust in the Wallowa Mountains probably has wet and mafic composition, making it susceptible to deformation.

In contrast, if the crust is cold and strong, mantle downwelling may induce prolonged surface subsidence and little internal crustal deformation. Many sedimentary basins are found in the cool interior regions of continents, and the evolution of such intracratonic basins is complex, with several episodes of subsidence. In some areas, the subsidence events are related to lithosphere extension, thermal subsidence and crustal buckling/folding (e.g. Lambeck 1983; Burg & Podladchikov 1999; Cloetingh *et al*. 2002; Schmalholz *et al*. 2002). In other basins, the subsidence mechanism is less clear, and some intracratonic basins have been linked to processes that originate in the mantle (e.g. Naimark & Ismail-Zadeh 1995). For example, the Congo basin in Africa formed by lithosphere extension in Latest Precambrian (Daly & Lawrence 1991). However, its later evolution is enigmatic as subsidence has continued for over 0.5 Ga (Crosby *et al*. 2010). Seismic tomography and free-air gravity data suggest the long subsidence history of the Congo basin in Africa may be related to downwelling mantle stresses. These stresses have been proposed to be caused by the presence of a high-density anomaly in deep lithosphere (Downey & Gurnis 2009) and/or the return (downward) flow of upwelling mantle at the flanks of the basin keel (Crosby *et al*. 2010). At present, the Congo basin remains as a topographic low and has no obvious thickened crust (Tedla *et al*. 2011), indicating that there has been little crustal deformation. This is consistent with the general thermal structure of this area, where low heat flow and seismic data indicate a cool, thick lithosphere (Sebagenzi *et al*. 1993). Without other tectonic processes, uplift in intracratonic basins may only occur once the downwelling mantle stresses are removed.

7 CONCLUSIONS

In this study, we have investigated the evolution of crustal deformation caused by stresses that originate in the mantle. In our models, a dense root is placed in mantle lithosphere and the models track how its gravitational removal affects the overlying crust. The models show that the process induces three main stresses on the crust: (1) a vertical normal stress owing to the negative buoyancy of the root, (2) a lateral pressure gradient that arises from the topographic variations created by the dense root and (3) a basal horizontal shear stress associated with the dynamical removal of the root. The first stress causes surface subsidence, while the latter two act to deform and thicken the crust, producing surface uplift. The overall topographic expression depends on the relative magnitude of these stresses (Fig. 12):

(1) If the crust is strong enough to resist deformation, the topographic expression directly reflects root dynamics (stress 1). Root removal creates surface subsidence, followed by uplift after the root detaches. During the whole process, the free-air gravity has a negative anomaly, mirroring the surface topography profile.

(2) If the crust contains a weak channel between two strong layers, the dense root can induce Poiseuille flow within the channel

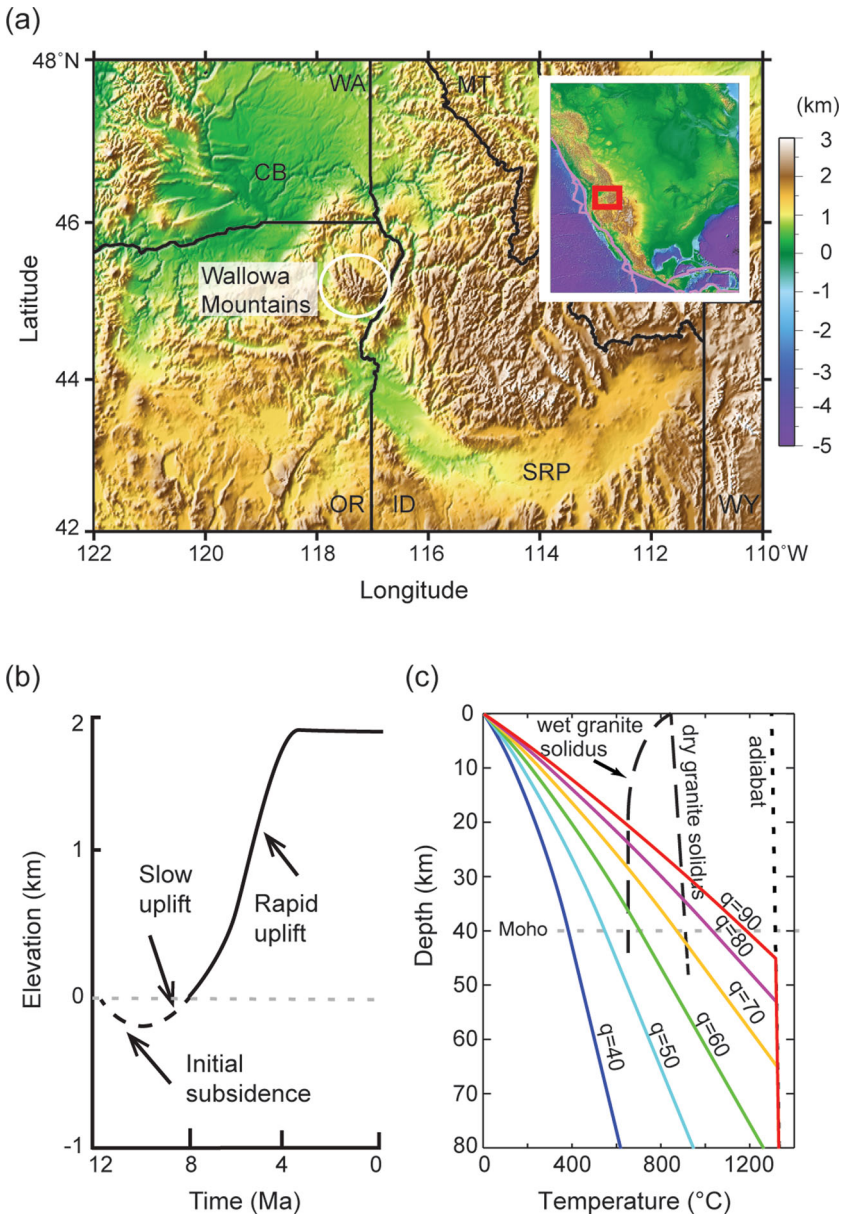

Figure 13. (a) Present-day surface topography in the Wallowa Mountains region (ETOPO1; Amante & Eakins 2009). CB = Columbia Basin; SRP = Snake River Plain; WA = Washington; OR = Oregon; ID = Idaho and MT = Montana. Insert map of North America shows the location of the Wallowa Mountains region. (b) Evolution of surface elevation (after Hales *et al*. 2005). (c) Geotherms for a 40 km crust for different surface heat flows (q, in mW m^{-2}). The thermal parameters are the same as those used for the geotherms in Fig. 1(b).

owing to lateral pressure variations (stress 2). This leads to crustal thickening and surface uplift while the root is undergoing removal (Fig. 12b). The maximum amount of uplift corresponds to the elevation of the adjacent regions that have no dense root. The free-air gravity has a minor anomaly in this case.

(3) If the lower crust is weak and is in direct contact with downwelling mantle, crustal deformation can occur due to both lateral pressure variations (stress 2) and basal shearing (stress 3). The crust thickens through a combination of Poiseuille and Couette flows (Fig. 12b). The basal shearing can overthicken the crust, creating a topographic high during root removal. Owing to the overthickened crust, free-air gravity anomaly remains negative even after the surface uplifts to a topographic high. In this case, surface uplift occurs, in spite of the negative dynamic topography caused by the downwelling mantle.

A strong crust may be found in areas of low heat flow. A mid-crustal channel may occur in warm, thick crust, in which the upper-mid crust has a rheologically weak composition (e.g. granite) and the lower crust has a strong mafic composition (e.g. dry diabase). A weak lower-crustal channel may be created if the deep crust is hot and has a felsic to intermediate composition. A weak lower crust may also occur in areas with an enhanced concentration of radioactive elements, crustal hydration and partial melting (e.g. Pysklywec & Beaumont 2004).

Our models demonstrate that under the same mantle-based stress, the resulting crustal thickness, surface topography and free-air gravity anomaly have different expressions depending on the crustal viscosity structure. This may explain the range of surface deflections observed above areas where lithospheric foundering has been proposed.

ACKNOWLEDGEMENTS

We thank Laetitia Le Pourhiet, Muriel Gerbault, Saskia Goes, two anonymous reviewers and editor Gaël Choblet for invaluable advice and comments. The numerical models in this study use the SOPALE numerical modeling code, developed under the direction of Dr Christopher Beaumont (Dalhousie University, Halifax NS). Research was supported by computational resources from Compute Canada (WestGrid) and a Discovery Grant from the Natural Sciences and Engineering Research Council of Canada (NSERC).

REFERENCES

Amante, C. & Eakins, B.W., 2009. *ETOPO1 1 Arc-Minute Global Relief Model: Procedures, Data Sources and Analysis,* NOAA Technical Memorandum NESDIS NGDC-24, 19 pp.

Beaumont, C., Jamieson, R.A., Nguyen, M.H. & Lee, B., 2001. Himalayan tectonics explained by extrusion of a low-viscosity crustal channel coupled to focused surface denudation, *Nature,* **414**(6865), 738–742.

Beaumont, C., Jamieson, R.A., Nguyen, M.H. & Medvedev, S., 2004. Crustal channel flows: 1. Numerical models with applications to the tectonics of the Himalayan-Tibetan orogeny, *J. geophys. Res.,* **109**(B6), doi:10.1029/2003JB002809.

Beaumont, C., Nguyen, M.H., Jamieson, R.A. & Ellis, S., 2006. Crustal flow modes in large hot orogens, *Geol. Soc. Lond. Spec. Publ.* **268,** 91–145.

Bird, P., 1991. Lateral extrusion of lower crust from under high topography in the isostatic limit, *J. geophys. Res.,* **96**(B6), 10 275–10 286.

Biryol, C.B., Wagner, L.S., Fischer, K.M. & Hawman, R.B., 2016. Relationship between observed upper mantle structures and recent tectonic activity across the Southeastern United States, *J. geophys. Res.,* **121,** 3393–3414.

Blackwell, D., Richards, M., Frone, Z., Ruzo, A., Dingwall, R. & Williams, M., 2011. Temperature-at-depth maps for the conterminous US and geothermal resource estimates, *Geotherm. Res. Counc. Trans.,* **35,** 1545–1550.

Braun, J., 2010. The many surface expressions of mantle dynamics, *Nat. Geosci.,* **3**(12), 825–833.

Buiter, S.J., Govers, R. & Wortel, M.J.R., 2002. Two-dimensional simulations of surface deformation caused by slab detachment, *Tectonophysics,* **354**(3), 195–210.

Burg, J.P. & Podladchikov, Y., 1999. Lithospheric scale folding: numerical modelling and application to the Himalayan syntaxes, *Int. J. Earth Sci.,* **88**(2), 190–200.

Burov, E. & Guillou-Frottier, L., 2005. The plume head–continental lithosphere interaction using a tectonically realistic formulation for the lithosphere, *Geophys J. Int.,* **161**(2), 469–490.

Burov, E.B. & Watts, A.B., 2006. The long-term strength of continental lithosphere: "jelly sandwich" or "crème brûlée"?, *GSA Today,* **16**(1), 4–10.

Burov, E.B. & Cloetingh, S., 2009. Controls of mantle plumes and lithospheric folding on modes of intraplate continental tectonics: differences and similarities, *Geophys J. Int.,* **178**(3), 1691–1722.

Chapman, D.S., 1986. Thermal gradients in the continental crust, *Geol. Soc. Lond. Spec. Publ.,* **24**(1), 63–70.

Christensen, N.I. & Mooney, W.D., 1995. Seismic velocity structure and composition of the continental crust: a global view, *J. geophys. Res.,* **100**(B6), 9761–9788.

Clark, M.K. & Royden, L.H., 2000. Topographic ooze: building the eastern margin of Tibet by lower crustal flow, *Geology,* **28**(8), 703–706.

Cloetingh, S., Burov, E., Beekman, F., Andeweg, B., Andriessen, P.A.M., Garcia Castellanos, D., de Vincente, G. & Vegas, R., 2002. Lithospheric folding in Iberia, *Tectonics,* **21**(5), doi:10.1029/2001TC901031.

Cloetingh, S., Burov, E.B. & Francois, T., 2013. Thermo-mechanical controls on intra-plate deformation and the role of plume-folding interactions in continental topography, *Gondwana Res.,* **24**(3), 815–837.

Conrad, C.P. & Molnar, P., 1999. Convective instability of a boundary layer with temperature-and strain-rate-dependent viscosity in terms of 'available buoyancy', *Geophys J. Int.,* **139**(1), 51–68.

Crosby, A.G., Fishwick, S. & White, N., 2010. Structure and evolution of the intracratonic Congo Basin, *Geochem. Geophys. Geosyst.,* **11**(6), doi:10.1029/2009GC003014.

Currie, C.A., Wang, K., Hyndman, R.D. & He, J., 2004. The thermal effects of steady-state slab-driven mantle flow above a subducting plate: the Cascadia subduction zone and backarc, *Earth planet. Sci. Lett.,* **223**(1), 35–48.

Daly, M.C. & Lawrence, S.R., 1991. Late palaeozoic deformation in central Africa: a result of distant collision?, *Nature,* **350**(6319), 605–607.

DeCelles, P.G., Carrapa, B., Horton, B.K., McNabb, J., Gehrels, G.E. & Boyd, J., 2015. The Miocene Arizaro Basin, central Andean hinterland: response to partial lithosphere removal?, *Geol. Soc. Am. Mem.,* **212,** 359–386.

Downey, N.J. & Gurnis, M., 2009. Instantaneous dynamics of the cratonic Congo basin, *J. geophys. Res.,* **114**(B6), doi:10.1029/2008JB006066.

Darold, A. & Humphreys, E., 2013. Upper mantle seismic structure beneath the pacific northwest: a plume-triggered delamination origin for the Columbia river flood basalt eruptions, *Earth planet. Sci. Lett.,* **365,** 232–242.

Ducea, M.N., 2001. The California arc: thick granitic batholiths, eclogitic residues, lithospheric-scale thrusting, and magmatic flare-ups, *GSA Today,* **11**(11), 4–10.

Ducea, M.N. & Saleeby, J.B., 1996. Buoyancy sources for a large, unrooted mountain range, the Sierra Nevada, California: evidence from xenolith thermobarometry, *J. geophys. Res.,* **101**(B4), 8229–8244.

Ducea, M.N., Seclaman, A.C., Murray, K.E., Jianu, D. & Schoenbohm, L.M., 2013. Mantle-drip magmatism beneath the Altiplano-Puna plateau, central Andes, *Geology,* **41**(8), 915–918.

Duretz, T., Schmalholz, S.M. & Gerya, T.V., 2012. Dynamics of slab detachment, *Geochem. Geophys. Geosyst.,* **13**(3), doi:10.1029/2011GC004024.

Elkins-Tanton, L.T., 2007. Continental magmatism, volatile recycling, and a heterogeneous mantle caused by lithospheric gravitational instabilities, *J. geophys. Res.,* **112,** B03405, doi:10.1029/2005JB004072.

Flament, N., Gurnis, M. & Müller, R.D., 2013. A review of observations and models of dynamic topography, *Lithosphere,* **5**(2), 189–210.

François, T., Burov, E., Meyer, B. & Agard, P., 2013. Surface topography as key constraint on thermo-rheological structure of stable cratons, *Tectonophysics,* **602,** 106–123.

Fullsack, P., 1995. Arbitrary lagrangian-eulerian formulation for creeping flows and its application in tectonic models, *Geophys. J. Int.,* **120**(1), 1–23.

Gao, S., Zhang, B.R., Jin, Z.M., Kern, H., Luo, T.C. & Zhao, Z.D., 1998. How mafic is the lower continental crust?, *Earth planet. Sci. Lett.,* **161**(1), 101–117.

Gao, H., Humphreys, E.D., Yao, H. & van der Hilst, R.D., 2011. Crust and lithosphere structure of the northwestern US with ambient noise tomography: terrane accretion and Cascade arc development, *Earth planet. Sci. Lett.,* **304**(1), 202–211.

Gemmer, L. & Houseman, G.A., 2007. Convergence and extension driven by lithospheric gravitational instability: evolution of the alpine–carpathian–pannonian system, *Geophys J. Int.,* **168**(3), 1276–1290.

Gerbault, M., Martinod, J., Hérail & G., 2005. Possible orogeny-parallel lower crustal flow and thickening in the Central Andes, *Tectonophysics,* **399**(1), 59–72.

Gleason, G.C. & Tullis, J., 1995. A flow law for dislocation creep of quartz aggregates determined with the molten salt cell, *Tectonophysics,* **247**(1), 1–23.

Göğüş, O.H. & Pysklywec, R.N., 2008. Near-surface diagnostics of dripping or delaminating lithosphere, *J. geophys. Res.,* **113,** B11404, doi:10.1029/2007JB005123.

Grujic, D., 2006. Channel flow and continental collision tectonics: an overview, *Geol. Soc. Lond. Spec. Publ.,* **268**(1), 25–37.

Gurnis, M., Müller, R.D. & Moresi, L., 1998. Cretaceous vertical motion of Australia and the Australian Antarctic discordance, *Science,* **279**(5356), 1499–1504.

Hales, T.C., Abt, D.L., Humphreys, E.D. & Roering, J.J., 2005. A lithospheric instability origin for columbia river flood basalts and wallowa mountains uplift in northeast oregon, *Nature,* **438**(7069), 842–845.

Hirth, G. & Kohlstedt, D.L., 1996. Water in the oceanic upper mantle: implications for rheology, melt extraction and the evolution of the lithosphere, *Earth planet. Sci. Lett.,* **144**(1), 93–108.

Hoogenboom, T. & Houseman, G.A., 2006. Rayleigh–Taylor instability as a mechanism for corona formation on venus, *Icarus,* **180**(2), 292–307.

Houseman, G.A. & Molnar, P., 1997. Gravitational (Rayleigh-Taylor) instability of a layer with non-linear viscosity and convective thinning of continental lithosphere, *Geophys J. Int.,* **128**(1), 125–150.

Houseman, G.A. & Molnar, P., 2001. Mechanisms of lithospheric rejuvenation associated with continental orogeny, *Geol. Soc. Lond. Spec. Publ.,* **184**(1), 13–38.

Houseman, G.A., McKenzie, D.P. & Molnar, P., 1981. Convective instability of a thickened boundary layer and its relevance for the thermal evolution of continental convergent belts, *J. geophys. Res.,* **86**(B7), 6115–6132.

Jamieson, R.A., Beaumont, C., Medvedev, S. & Nguyen, M.H., 2004. Crustal channel flows: 2. Numerical models with implications for metamorphism in the Himalayan Tibetan orogeny, *J. geophys. Res.,* **109**(B6), doi:10.1029/2003JB002809.

Jamieson, R.A., Beaumont, C., Nguyen, M.H. & Grujic, D., 2006. Provenance of the Greater Himalayan Sequence and associated rocks: predictions of channel flow models, *Geol. Soc. Lond. Spec. Publ.,* **268**(1), 165–182.

Jull, M. & Kelemen, P.B., 2001. On the conditions for lower crustal convective instability, *J. geophys. Res.,* **106**(B4), 6423–6446.

Kay, R.W. & Kay, S.M., 1993. Delamination and delamination magmatism, *Tectonophysics,* **219,** 177–189.

Kohlstedt, D.L., Evans, B. & Mackwell, S.J., 1995. Strength of the lithosphere: constraints imposed by laboratory experiments, *J. geophys. Res.,* **100**(B9), 17587–17602.

Kreemer, C., Holt, W.E. & Haines, A.J., 2003. An integrated global model of present-day plate motions and plate boundary deformation, *Geophys J. Int.,* **154**(1), 8–34.

Kruse, S., McNutt, M., Phipps-Morgan, J., Royden, L. & Wernicke, B., 1991. Lithospheric extension near Lake Mead, Nevada: a model for ductile flow in the lower crust, *J. geophys. Res.,* **96**(B3), 4435–4456.

Kusznir, N.J. & Park, R.G., 1984. Intraplate lithosphere deformation and the strength of the lithosphere, *Geophys J. Int.,* **79**(2), 513–538.

Lambeck, K., 1983. Structure and evolution of the intracratonic basins of central Australia,*Geophys. J. R. astr. Soc.,* **74**(3), 843–886.

Levandowski, W. & Jones, C.H., 2015. Linking Sierra Nevada, California, uplift to subsidence of the Tulare basin using a seismically derived density model, *Tectonics,* **34**(11), 2349–2358.

Li, S., Unsworth, M.J., Booker, J.R., Wei, W., Tan, H. & Jones, A.G., 2003. Partial melt or aqueous fluid in the mid-crust of Southern Tibet? Constraints from INDEPTH magnetotelluric data, *Geophys. J. Int.,* **153**(2), 289–304.

Mackwell, S.J., Zimmerman, M.E. & Kohlstedt, D.L., 1998. High-temperature deformation of dry diabase with application to tectonics on Venus, *J. geophys. Res.,* **103**(B1), 975–984.

Makovsky, Y., Klemperer, S.L., Huang, L. & Lu, D., 1996. Structural elements of the southern Tethyan Himalaya crust from wide-angle seismic data, *Tectonics,* **15**(5), 997–1005.

Mazzotti, S. & Hyndman, R.D., 2002. Yakutat collision and strain transfer across the northern Canadian Cordillera, *Geology,* **30**(6), 495–498.

McKenzie, D., 1977. Surface deformation, gravity anomalies and convection, *Geophys. J. Int.,* **48**(2), 211–238.

McQuarrie, N. & Chase, C. G., 2000. Raising the colorado plateau, *Geology,* **28**(1), 91–94.

Molnar, P. & Houseman, G.A., 2013. Rayleigh-Taylor instability, lithospheric dynamics, surface topography at convergent mountain belts, and gravity anomalies, *J. geophys. Res.,* **118**(5), 2544–2557.

Molnar, P. & Houseman, G.A., 2015. Effects of a low viscosity lower crust on topography and gravity at convergent mountain belts during gravitational instability of mantle lithosphere, *J. geophys. Res.,* **120,** 537–551.

Moresi, L. & Lenardic, A., 1999. Three-dimensional mantle convection with continental crust: first-generation numerical simulations, *Earth Interact.,* **3**(2), 1–14.

Morgan, W.J., 1965. Gravity anomalies and convection currents: 1. A sphere and cylinder sinking beneath the surface of a viscous fluid, *J. geophys. Res.,* **70**(24), 6175–6187.

Naimark, B.M. & Ismail-Zadeh, A.T., 1995. Numerical models of a subsidence mechanism in intracratonic basins: application to North American basins, *Geophys J. Int.,* **123**(1), 149–160.

Neil, E.A. & Houseman, G.A., 1999. Rayleigh-Taylor instability of the upper mantle and its role in intraplate orogeny, *Geophys J. Int.,* **138**(1), 89–107.

Nelson, K.D., Zhao, W., Brown, L.D., Kuo, J., Che, J., Liu, X. & Edwards, M., 1996. Partially molten middle crust beneath southern Tibet: synthesis of project INDEPTH results, *Science,* **274**(5293), 1684–1688.

Petit, C., Le Pourhiet, L., Scalabrino, B., Corsini, M., Bonnin, M. & Romagny, A., 2015. Crustal structure and gravity anomalies beneath the Rif, northern Morocco: implications for the current tectonics of the Alboran region, *Geophys. J. Int.,* **202**(1), 640–652.

Poudjom Djomani, Y.H., O'Reilly, S.Y., Griffin, W.L. & Morgan, P., 2001. The density structure of subcontinental lithosphere through time, *Earth planet. Sci. Lett.,* **184**(3), 605–621.

Pysklywec, R.N. & Shahnas, M.H., 2003. Time-dependent surface topography in a coupled crust–mantle convection model, *Geophys. J. Int.,* **154**(2), 268–278.

Pysklywec, R.N. & Beaumont, C., 2004. Intraplate tectonics: feedback between radioactive thermal weakening and crustal deformation driven by mantle lithosphere instabilities, *Earth planet. Sci. Lett.,* **221**(1), 275–292.

Ranalli, G., 1995. *Rheology of the Earth,* 2nd edn, Chapman & Hall.

Ranalli, G. & Murphy, D.C., 1987. Rheological stratification of the lithosphere, *Tectonophysics,* **132**(4), 281–295.

Richards, J.P., 2003, Tectono-magmatic precursors for porphyry Cu-(Mo-Au) deposit formation, *Econ. Geol.,* **98**(8), 1515–1533.

Rippe, D. & Unsworth, M., 2010. Quantifying crustal flow in Tibet with magnetotelluric data, *Phys. Earth planet Inter.,* **179**(3), 107–121.

Rosenberg, C.L. & Handy, M.R., 2005. Experimental deformation of partially melted granite revisited: implications for the continental crust, *J. Metamorph. Geol.,* **23**(1), 19–28.

Royden, L.H., Burchfiel, B.C. & van der Hilst, R.D., 2008. The geological evolution of the Tibetan Plateau, *Science,* **321**(5892), 1054–1058.

Saleeby, J., Ducea, M.N. & Clemens-Knott, D., 2003. Production and loss of high-density batholithic root, southern Sierra Nevada, California, *Tectonics,* **22**(6), 1064, doi:10.1029/2002TC001374.

Saleeby, J., Le Pourhiet, L., Saleeby, Z. & Gurnis, M., 2012. Epeirogenic transients related to mantle lithosphere removal in the southern Sierra Nevada region, California, Part I: Implications of thermomechanical modeling, *Geosphere,* **8**(6), 1286–1309.

Schmalholz, S.M., Podladchikov, Y.Y. & Burg, J.P., 2002. Control of folding by gravity and matrix thickness: implications for large scale folding, *J. geophys. Res.,* **107**(B1), doi:10.1029/2001JB000355.

Schoenbohm, L.M. & Carrapa, B., 2014. Miocene–Pliocene shortening, extension, and mafic magmatism support small-scale lithospheric foundering in the central Andes, NW Argentinae, *Geol. Soc. Am. Mem.,* **212,** MWR212-09.

Sebagenzi, M.N., Vasseur, G. & Louis, P., 1993. First heat flow density determinations from southeastern Zaire (central Africa). *J. Afr. Earth Sci.,* **16**(4), 413–423.

Talwani, M., Worzel, J.L. & Landisman, M., 1959. Rapid gravity computations for two dimensional bodies with application to the Mendocino submarine fracture zone, *J. geophys. Res.,* **64**(1), 49–59.

Tedla, G.E., Van Der Meijde, M., Nyblade, A.A. & Van der Meer, F.D., 2011. A crustal thickness map of Africa derived from a global gravity field model using Euler deconvolution, *Geophys. J. Int.,* **187**(1), 1–9.

Turcotte, D.L. & Schubert, G., 2002. *Geodynamics,* 2nd edn, Cambridge Univ. Press.

Wang, Y.F., Zhang, J.F., Jin, Z.M. & Green, H.W., 2012. Mafic granulite rheology: implications for a weak continental lower crust, *Earth planet. Sci. Lett.,* **353,** 99–107.

Wang, H., Currie, C.A. & Zhan, Y., 2014. Surface expressions of Rayleigh Taylor instability in continental interiors, *Acta Geol. Sin. (English Edition),* **88**(3), 1004–1016.

Wang, H., Currie, C.A. & DeCelles, P.G., 2015. Hinterland basin formation and gravitational instabilities in the central Andes: constraints from gravity data and geodynamic models, *Geol. Soc. Am. Mem.,* **212,** 387–406.

Whitehead, J.A. & Luther, D.S., 1975. Dynamics of laboratory diapir and plume models, *J. geophys. Res.,* **80**(5), 705–717.

APPENDIX A: ANALYSIS OF CRUSTAL CHANNEL FLOW

The numerical models in this study show that lateral crustal flow can be induced by gravitational lithosphere removal (Figs 7 and 8). Here, we use a theoretical analysis to demonstrate the origin for crustal flow. In the analysis, the crust and mantle have constant densities and constant viscosities, as in the numerical models. This allows for a simplified treatment of the relationship between of root foundering and deformation of the crustal channel.

A1 Mid-crustal channel

We first consider a ductile channel in the mid-crust (Fig. A1a). The upper and lower crusts are assumed to be too strong to be deformed internally. The presence of the dense root in the mantle lithosphere induces a vertical normal stress on the lithosphere, generating an initial downward surface deflection above the root. This creates a topographic gradient at the surface and leads to a horizontal pressure gradient within the crust. Here, the pressure gradient refers to a lateral difference in the lithostatic pressure profile between two regions that have different surface elevations (Grujic 2006). As a result, areas of low elevation have a lower pressure. If the crust is sufficiently weak, the crust will flow toward the low pressure region, in order to reduce the pressure gradient (e.g. Bird 1991; Kruse *et al*. 1991; Grujic 2006).

For a mid-crustal channel, the channel deforms through Poiseuille flow, and the average channel velocity $\bar{v}$ can be expressed as (Turcotte & Schubert 2002):

$$\bar{v} = -\frac{{h_{\rm ch}}^2}{12\eta_{\rm ch}}\frac{dP}{dx} \tag{A1}$$

where $\eta_{\rm ch}$ and $h_{\rm ch}$ are the viscosity and thickness of channel, respectively, and $\frac{dP}{dx}$ is the horizontal pressure gradient. The negative sign is due to the fact that the velocity is in the direction of decreasing pressure gradient. In the coordinate system of our models, a negative velocity means materials are moving towards the left model boundary ($x = 0$ km); this is consistent with this region being an area of low topography, and thus low pressure, at the start of phase 2 of the models.

In our models, the horizontal pressure gradient arises from the surface topographic deflection caused by the presence of the high-density root. Following Kruse *et al*. (1991), the initial pressure gradient can be written as:

$$\frac{dP}{dx} \approx -\frac{\rho_c g S_{\rm sub}}{L_{\rm basin}} \tag{A2}$$

where $\rho_{\rm c}$ is the crustal density, g is the gravitational acceleration and $S_{\rm sub}$ is surface deflection ($S_{\rm sub} < 0$ km corresponds to lower topography at $x = 0$ km compared to regions to the right). $L_{\rm basin}$ is the half-width of the basin (Fig. A1a). In our models, $L_{\rm basin}$ is approximately half of the horizontal length of the region that undergoes crustal flow, $L_{\rm flow}$ ($L_{\rm basin} \approx 0.5 \times L_{\rm flow}$). In Fig. 9, $L_{\rm basin} = 150$ km is used for Models B and C.

The pressure gradient drives flow toward the area above the dense root, resulting in crustal thickening above the root. If the crust here thickens by Δh, then according to Airy isostatic compensation, the surface will uplift by $\Phi\Delta h$ (where $\Phi = (\rho_m - \rho_c)/\rho_m$, and $\rho_{\rm m}$ is the mantle density) and the lower boundary of the crust (the Moho) will be pushed downward by $(1 - \Phi)\Delta h$, due to the weight of the thickened crust (Kruse *et al*. 1991; Turcotte & Schubert 2002). Thus, the surface topography that drives channel flow depends on

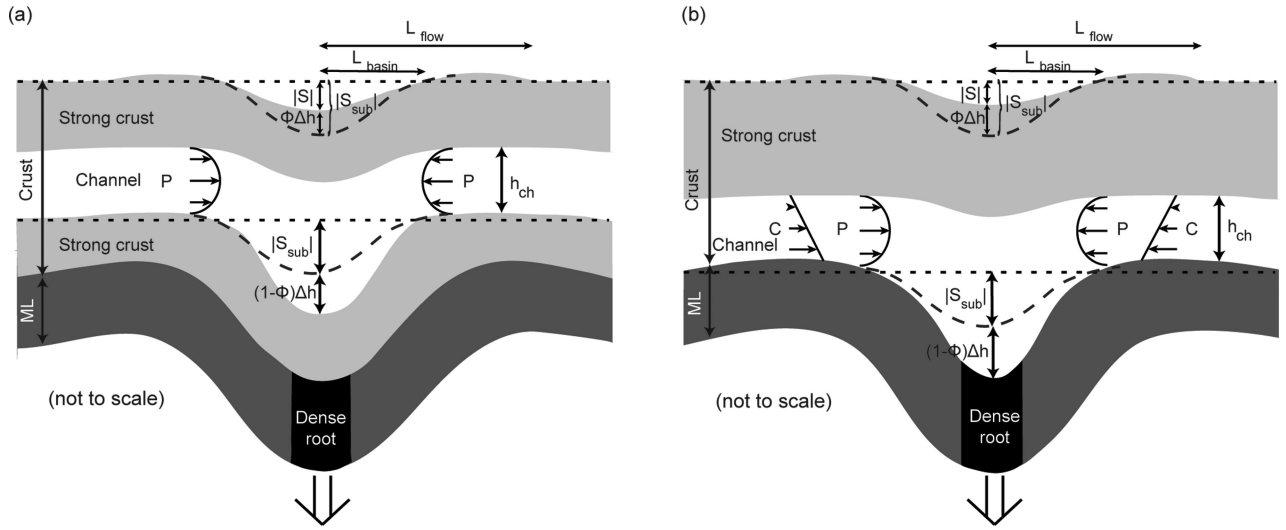

Figure A1. Schematic diagram illustrating the crustal deformation during gravitational removal of a dense root (black block). (a) For a weak mid-crustal channel (thickness $h_{\rm ch}$), bounded by strong upper crust and lower crust, Poiseuille flow (P) is induced in the channel. (b) For a weak lower-crustal channel (thickness $h_{\rm ch}$), which is directly coupled with the mantle lithosphere (ML), deformation consists of both Poiseuille flow (P) and Couette flow (C). $S_{\rm sub}$ is the initial surface elevation at $x = 0$ km caused by isostatic and dynamic stresses from the dense root (shown with dashed lines); S is surface deflection after the onset of channel flow; Δh is the amount of crustal thickening due to channel flow; $\Phi = (\rho_m - \rho_c)/\rho_m$, where ρ_m is mantle density and ρ_c is crust density. The dotted lines show the surface elevation and lower boundary of the channel outside the area of deformation. $L_{\rm basin}$ is the half-width of basin. $L_{\rm flow}$ is the horizontal length of crustal flow in channel. See the text for details.

both the dense root and the induced crustal thickening, with a total surface deflection above the root of:

$$S = S_{\text{sub}} + \Phi \Delta h \tag{A3}$$

The pressure gradient in the channel can then be written as:

$$\frac{dP}{dx} \approx -\frac{\rho_c g S}{L_{\text{basin}}}. \tag{A4}$$

Combining eqs (A1) and (A4), the average velocity of channel flow is:

$$\bar{v} \approx \frac{{h_{\text{ch}}}^2}{12\eta_{\text{ch}}} \rho_c g \frac{S}{L_{\text{basin}}}. \tag{A5}$$

This equation predicts the average velocity of channel flow within a mid-crustal channel (i.e. one bounded by strong layers) due to a topographic deflection of S. Note that in the coordinate system of our models, when there is a topographic low above the root, S is negative and the channel flow is directed toward the root.

A2 Lower-crustal channel

If the weak channel is located in the lower crust, we assume its upper boundary (upper-mid crust) is strong and cannot be deformed laterally (Fig. A1b). The lower boundary is directly attached to the mantle and can be sheared as the dense root is removed. Therefore, the channel has zero velocity on its upper boundary, but a non-zero velocity on its lower boundary.

As the dense root founders, it entrains the adjacent mantle lithosphere, causing shear along the base of the channel towards the dense root. The relative motion between the upper and lower channel boundaries induces Couette flow in the channel, with an average velocity of (Turcotte & Schubert 2002):

$$\bar{v}_c = \frac{1}{2} v_0 \tag{A6}$$

where v_0 is the horizontal velocity of the lower boundary.

In addition to Couette flow, the channel experiences Poiseuille flow associated with the lateral pressure gradient induced by the surface topography variations, as discussed above. Therefore, the net velocity of the lower-crustal channel is the sum of eqs (A5) and (A6):

$$\bar{v} \approx \frac{{h_{\text{ch}}}^2 \rho_c g S}{12\eta_{\text{ch}} L_{\text{basin}}} + \frac{1}{2} v_0. \tag{A7}$$

In this case, the channel flow velocity is driven by both the topographic gradient and shear on the lower boundary of the channel. In the coordinate system of our models, the centre root is located at $x = 0$ km, and the basal shear is in the negative x-direction, meaning that the second term is always negative. The pressure-driven flow (first term) will be in the positive or negative x-direction, depending on whether the region above the root centre is a topographic high (positive S) or low (negative S), respectively.